# Endwall Heat Transfer and Shear Stress for a Nozzle Guide Vane with Fillets and a Leakage Interface

Stephen P. Lynch

Thesis submitted to the Faculty
of Virginia Polytechnic Institute and State University
in partial fulfillment of the requirements for the degree of

Master of Science
in
Mechanical Engineering

Dr. Karen Thole, Chair
Dr. Wing Ng
Dr. Brian Vick

April 18, 2007
Blacksburg, VA

Keywords: gas turbines, vane endwalls,
film-cooling, fillets

# Endwall Heat Transfer and Shear Stress for a Nozzle Guide Vane with Fillets and a Leakage Interface

**Stephen P. Lynch**

## Abstract

Increasing the combustion temperatures in a gas turbine engine to achieve higher efficiency and power output also results in high heat loads to turbine components downstream of the combustor. The challenge of adequately cooling the nozzle guide vane directly downstream of the combustor is compounded by a complex vortical secondary flow at the junction of the endwall and the airfoil. This flow tends to increase local heat transfer rates and sweep coolant away from component surfaces, as well as decrease the turbine aerodynamic efficiency. Past research has shown that a large fillet at the endwall-airfoil junction can reduce or eliminate the secondary flow. Also, leakage flow from the interface gap between the combustor and the turbine can provide some cooling to the endwall. This study examines the individual and combined effects of a large fillet and realistic combustor-turbine interface gap leakage flow for a nozzle guide vane. The first study focuses on the effect of leakage flow from the interface gap on the endwall upstream of the vane. The second study addresses the influence of large fillets at the endwall-airfoil junction, with and without upstream leakage flow. Both studies were performed in a large low-speed wind tunnel with the same vane geometry. Endwall shear stress measurements were obtained for various endwall-airfoil junction geometries without upstream leakage flow. Endwall heat transfer and cooling effectiveness were measured for various leakage flow rates and leakage gap widths, with a variety of endwall-airfoil junction geometries.

Results from these studies indicate that the secondary flow has a large influence on the coverage area of the leakage coolant. Increased leakage flow rates resulted in better cooling effectiveness and coverage, but also higher heat transfer rates. The two fillet geometries tested affected coolant coverage by displacing coolant around the base of the fillet, which could result in undesirably high gradients in endwall temperature. The addition of a large fillet to the endwall-airfoil junction, however, reduced heat transfer, even when upstream leakage flow was present.

## Attribution

The co-author for Paper 1, entitled, "The Effect of Combustor-Turbine Interface Gap Leakage on the Endwall Heat Transfer for a Nozzle Guide Vane", is Dr. Karen Thole. Dr. Thole is affiliated with the Mechanical and Nuclear Engineering Department at The Pennsylvania State University in University Park, PA. Her contribution to the work presented in Paper 1 included general advising on the experimental setup and data analysis, as well as editing of the manuscript.

Dr. Karen Thole is also a co-author for Paper 2, entitled, "Heat Transfer and Shear Stress for a Nozzle Guide Vane Endwall with Fillets and Combustor-Turbine Gap Leakage Flow". Her contribution to the work presented in Paper 2 included manuscript editing, and advice with the design of the experiment and analysis of the results.

## Acknowledgments

I would like to sincerely thank all who have helped me achieve this milestone in my life. First and foremost is my rock, Jesus Christ, who gives me joy for the good times, and strength for the hard times. All of my blessings and achievements are from Him, and although the road can be hard to follow, I know He has a plan. I would like to thank my family, beginning with the best thing that has ever happened to me: my wife Becca. I will never be able to tell you how much you mean to me. The fact that we have created life together is the best expression of my love for you. I would also like to thank my parents Pat and Cathy, and my siblings Liz, Kevin, Michelle, and Brian. Without their love, encouragement, and constant teasing (!), I would not be the person I am today. I am blessed to be in the company of such good people.

Many, many thanks are due to my advisor, Karen Thole. You have provided me with many opportunities and challenges, but more importantly, you have believed in my abilities. I very much appreciate your guidance and patience as I have grown in my professional life, and I am looking forward to the next chapter in our time together. You are a role model for me and I hope that someday I can give my graduate students the types of opportunities that you have given to me.

My labmates are last here but certainly not least. All of the good people who have come and gone from VTExCCL have left an impression on me that I will not forget. My life has been changed forever by your friendship, and thanks are not enough. All of my memories of you are fond ones: LabCathlon, Music Night, the white t-shirt mob all sleeping in class, Princess Chicken, noontime basketball, lunch at El Rod's/Rivermill/Hunan/any other seedy but cheap food place, and many others…thanks to all of you, and God bless you all.

## Table of Contents


Abstract ..... ii
Attribution ..... iii
Acknowledgments ..... iv
List of Tables ..... vii
List of Figures ..... viii
Preface ..... xi

Paper 1: The Effect of Combustor-Turbine Interface Gap Leakage on the Endwall Heat Transfer for a Nozzle Guide Vane ..... 1
- Abstract ..... 1
- Introduction ..... 2
- Relevant Past Studies ..... 2
- Experimental Facility and Methodology ..... 4
  - i. Endwall Friction Coefficient Measurements ..... 6
  - ii. Adiabatic Effectiveness Measurements ..... 8
  - iii. Heat Transfer Measurements ..... 9
- Discussion of Results ..... 10
  - i. Friction Coefficients without an Upstream Slot ..... 10
  - ii. Adiabatic Effectiveness Levels from an Upstream Slot ..... 11
  - iii. Heat Transfer Coefficients for an Upstream Slot ..... 14
  - iv. Net Heat Flux Reduction for an Upstream Slot ..... 15
- Conclusions ..... 17
- Acknowledgments ..... 18
- Nomenclature ..... 18
- References ..... 19

Paper 2: Heat Transfer and Shear Stress for a Nozzle Guide Vane Endwall with Fillets and Combustor-Turbine Gap Leakage Flow ..... 31
- Abstract ..... 31
- Introduction ..... 32
- Relevant Past Studies ..... 33
- Experimental Facility and Methodology ..... 35
  - i. Combustor-Turbine Interface Geometry ..... 36
  - ii. Endwall-Airfoil Fillet Designs ..... 37
  - iii. Shear Stress Measurements ..... 37
  - iv. Heat Transfer Coefficient Measurements ..... 39
  - v. Adiabatic Effectiveness Measurements ..... 40
- Discussion of Results ..... 41
  - i. Wall Shear Stress without an Upstream Slot ..... 41
  - ii. Heat Transfer Coefficients without an Upstream Slot ..... 42
  - iii. Heat Transfer Coefficients with Upstream Slot Flow ..... 44
  - iv. Adiabatic Effectiveness Levels from an Upstream Slot ..... 46

Conclusions....48
Acknowledgments....49
Nomenclature....49
References....50

## List of Tables


Table 1.1 Vane Geometry and Flow Conditions....22

Table 1.2 Inlet Boundary Layer Characteristics....22

Table 1.3 Slot Coolant Settings....22

Table 2.1 Vane Geometry and Flow Conditions....54

Table 2.2 Leakage Flow Coolant Settings....54

Table 2.3 Endwall and Fillet Geometry....54

## List of Figures


Figure 1.1 Large low-speed wind tunnel with separate flow conditioning paths and corner test section ..... 23

Figure 1.2 A schematic of the endwall and the combustor-turbine leakage interface (upstream slot) modeled in this study ..... 23

Figure 1.3 Example of oil film interferograms on nickel foil, used to determine endwall friction coefficient magnitude and direction ..... 24

Figure 1.4 Measured friction coefficient vectors for no upstream slot flow, which illustrate the features of secondary flow over the endwall ..... 24

Figure 1.5 Endwall limiting streamlines and the separation line (blue) calculated from the friction coefficient vectors in Figure 1.4, with inviscid streamlines (red) from FLUENT [21] overlaid ..... 25

Figure 1.6a-d Contours of endwall effectiveness from upstream slot flow for (a) nominal slot, MFR=0.5%; (b) half slot, MFR=0.5%; (c) nominal slot, MFR=1.0%; (d) half slot, MFR=1.0% ..... 25

Figure 1.7a-c Adiabatic cooling effectiveness on the endwall from upstream slot flow, sampled along an inviscid streamline released from (a) 25% pitch, (b) 50% pitch, (c) 75% pitch ..... 26

Figure 1.8a-b Contours of effectiveness for the nominal slot at 1.0% MFR for (a) Knost & Thole [10] (slot at $X/C_{ax}$=-0.38), and (b) this study (slot at $X/C_{ax}$=-0.77) ..... 26

Figure 1.9a-f Contours of St for (a) Kang et al. [5] (no upstream slot); (b) baseline (no upstream slot); (c) nominal slot, MFR=0.5%; (d) half slot, MFR=0.5%; (e) nominal slot, MFR=1.0%; (f) half slot, MFR=1.0% ..... 27

Figure 1.10a-c Heat transfer augmentation on the endwall from upstream slot flow, sampled along an inviscid streamline released from (a) 25% pitch, (b) 50% pitch, (c) 75% pitch ..... 28

Figure 1.11a-c Heat transfer augmentation on the endwall from upstream slot flow, sampled along an inviscid streamline released from (a) 25% pitch, (b) 50% pitch, (c) 75% pitch ..... 29

Figure 1.12 Area-averaged net heat flux reduction (NHFR) to the endwall, as a function of upstream slot momentum flux ratio .....30

Figure 2.1 Depiction of the closed loop wind tunnel used in this study .....55

Figure 2.2 Schematic of the endwall and combustor-turbine interface gap (upstream slot) modeled in this study .....55

Figure 2.3a-b Geometrical parameters for an endwall-airfoil fillet with (a) a linear profile, and (b) an elliptical profile .....56

Figure 2.4a-b Schematic of oil film development due to shear (a); and a sample interferogram (b) which demonstrates friction coefficient directionality.....57

Figure 2.5a-b Friction coefficient magnitude for a vane with (a) no fillet, and with (b) a linear fillet.....57

Figure 2.6 Endwall streamlines for the linear fillet (black), overlaid with unfilleted endwall streamlines (red). Streamlines were calculated from the surface shear stress measurements .....58

Figure 2.7 Yaw angle of endwall streamlines at the throat compared to inviscid streamlines, indicating reduced overturning for a vane with a linear fillet .....58

Figure 2.8a-b Computed flowfield results of Lethander et al. [6] at plane SS2 with (a) no fillet, and (b) the linear fillet.....59

Figure 2.9a-b Heat transfer coefficient contours for the endwall (a) without a fillet, and (b) with the linear fillet. Inviscid streamline paths are overlaid on (a).....59

Figure 2.10 Heat transfer coefficients without upstream slot blowing, extracted along the inviscid streamline approaching the vane stagnation (see Figure 2.9a).....60

Figure 2.11 Heat transfer coefficients at the throat for no upstream slot blowing.....60

Figure 2.12a-h Heat transfer coefficient contours for the various upstream slot flow rates and widths, for the endwall without a fillet (a-d) and the endwall with a linear fillet (e-h) .....61

Figure 2.13 Heat transfer augmentation relative to the no-blowing cases, extracted along the 0.50P streamline path, for increased slot mass flow through the nominal slot....62

Figure 2.14 Heat transfer augmentation along the 0.50P streamline path for matched slot momentum flux from the nominal and half slots....62

Figure 2.15 Heat transfer augmentation for the linear fillet along the inviscid stagnation (STAG) streamline path....63

Figure 2.16 Comparison of area-averaged heat transfer for the various upstream slot leakage flow conditions....63

Figure 2.17a-l Adiabatic cooling effectiveness contours for the various upstream slot flow rates and widths, for an airfoil with no fillet (a-d), a linear fillet (e-h), and an elliptical fillet (i-l)....64

Figure 2.18 Adiabatic cooling effectiveness for low slot leakage mass flow, along the inviscid streamline path approaching the vane stagnation....65

Figure 2.19 Cooling effectiveness levels extracted along the 0.50P streamline for matched slot momentum flux ratio....65

Figure 2.20 Area-averaged adiabatic cooling effectiveness of leakage flow from an upstream slot, for an airfoil with no fillet, a linear fillet, or an elliptical fillet....66

## Preface

Turbine efficiency and power output are directly related to an increase in the temperature entering the turbine section. However, turbine component durability is adversely affected by increased temperatures. Advanced cooling schemes are necessary for part survival, but require the use of high-pressure air bypassed from the compressor section. This reduces engine efficiency, and minimal use of the bypass air is desirable. One such use of the bypass air is leakage through interface gaps between turbine components, to prevent hot gas ingestion. Leakage flow from the gap between the combustor and the turbine can also provide some cooling to the endwall of the nozzle guide vane; however, the endwall cooling is complicated by a vortical secondary flow at the endwall-airfoil junction, which can sweep coolant away from the endwall and increase heat transfer. A large leading edge fillet at the endwall-airfoil junction has been shown to mitigate the effect of the secondary flow, but the combined effect of gap leakage flow and the fillet has not been studied. It is hypothesized that the fillet will reduce endwall heat transfer, even in the presence of leakage flow, because of its effect on the secondary flow. Included are two papers which analyze the individual and combined effects of upstream leakage flow and large leading-edge endwall-airfoil fillet designs.

The first paper is entitled, “The Effect of Combustor-Turbine Interface Gap Leakage on the Endwall Heat Transfer for a Nozzle Guide Vane”. Measurements of endwall shear stress, heat transfer, and cooling effectiveness were presented for a nozzle guide vane with leakage flow from a realistic combustor-turbine interface gap upstream of the vanes. The gap location was moved much farther upstream than in other studies, which negatively impacted cooling effectiveness levels in the passage but resulted in more uniform coverage upstream of the vane. The endwall streamline topology without leakage flow correlated well with the leakage coolant coverage pattern, suggesting that the vortical secondary flow at the endwall-airfoil junction strongly influences the coolant trajectory through the passage. A reduction in the leakage gap width, simulating engine axial thermal expansion, resulted in lower cooling effectiveness but also lower heat transfer.

The second paper is entitled, “Heat Transfer and Shear Stress for a Nozzle Guide Vane Endwall with Fillets and Combustor-Turbine Gap Leakage Flow”. This study examined the individual and combined effects of large leading-edge endwall-airfoil fillets and combustor-

turbine interface gap leakage flow through measurements of endwall shear stress, heat transfer, and leakage flow cooling effectiveness for a nozzle guide vane. The addition of a fillet to the endwall-airfoil junction increased endwall shear stress and heat transfer at the throat of the vane cascade, but also reduced overall average heat transfer to the endwall relative to an unfilleted endwall. This benefit of reduced endwall heat transfer with a fillet was also apparent when upstream leakage flow was present. Unfortunately, both the linear and elliptical fillet geometries tested resulted in decreased coolant coverage and effectiveness levels compared to an unfilleted endwall.

## Paper 1:

# THE EFFECT OF COMBUSTOR-TURBINE INTERFACE GAP LEAKAGE ON THE ENDWALL HEAT TRANSFER FOR A NOZZLE GUIDE VANE

Accepted to the ***2007 IGTI Conference****
Recommended for publication in the ***Journal of Turbomachinery****

## Abstract

To enable turbine components to withstand high combustion temperatures, they are cooled by air routed from the compressor, which can leak through gaps between components. These gaps vary in size from thermal expansions that take place. The leakage flow between the interface of the combustor and the turbine, in particular, interacts with the flowfield along the endwall.

This study presents measurements of adiabatic cooling effectiveness and heat transfer coefficients on the endwall of a first vane, with the presence of leakage flow through a flush slot upstream of the vane. The effect of axial contraction of the slot width due to thermal expansion of the engine was tested for two blowing rates. Contracting the slot width, while maintaining the slot mass flow, resulted in a larger coolant coverage area and higher effectiveness values, as well as slightly lower heat transfer coefficients. Matching the momentum flux ratio of the leakage flow from the nominal and contracted slot widths lowered both cooling effectiveness and heat transfer coefficients for the contracted slot flow. Comparison of the coolant coverage pattern to the measured endwall shear stress topology indicated that the trajectory of the slot coolant was dictated by the complex endwall flow.

*Co-author: Dr. Karen A. Thole, Mechanical and Nuclear Engineering Department, The Pennsylvania State University

## Introduction

To achieve high efficiency and maximum power output, the temperature of the combustion gases entering the turbine section of a gas turbine engine must be as high as possible, while acknowledging the limitations of material strength and durability. This subjects the turbine section components to high heat loads which must be managed by cooling, since turbine inlet temperatures are generally well above the melting point of the metal. Relatively cool air is bled from the compressor and routed to the turbine components, where it provides internal and external cooling. Cooling is particularly important on the endwall of a turbine vane or blade, since the complex flow in that region results in high heat transfer rates, and also tends to sweep coolant away from the endwall surface.

Assembly of individual turbine components inherently results in gaps between parts. The large operational range of a gas turbine results in significant thermal expansion, making these gaps difficult to seal. Furthermore, the temperature profile exiting the combustor may not be uniform, leading to additional thermal expansion issues. Since leakage of the hot combustion gases into the gaps is detrimental to engine durability, high-pressure compressor bleed air is purged through the gaps. Purge flow, however, results in a loss in turbine efficiency since it does no useful work, and it is desirable to minimize this flow.

One gap that must be considered is between the combustor and the first stage of the turbine section. In addition to preventing hot gas ingestion, purge flow through the combustor-turbine interface gap can provide some cooling to the endwall of the turbine vane. However, the trajectory of this coolant is influenced by the complex endwall flowfield. Thermal expansion of the combustor-turbine interface gap during engine operational cycling also influences purge flow and changes the heat transfer experienced by the endwall.

This paper discusses the effects of leakage flow on turbine vane endwall heat transfer, for a combustor-turbine interface gap with axial thermal expansion. Also considered is the effect of moving the interface far upstream of the turbine vanes.

## Relevant Past Studies

The endwall flowfield of a first stage turbine vane consists of unique features that contribute to high heat transfer and aerodynamic losses. Although there are slight differences in detail, flowfield studies by Langston et al. [1], Sharma and Butler [2], Goldstein and Spores [3],

and others concur on the dominant structures in the endwall region for an approach flow that is uniform with a two-dimensional boundary layer. The incoming boundary layer on the endwall rolls up into a horseshoe vortex at the leading edge of the vane. The horseshoe vortex splits into suction and pressure side legs where the pressure side leg develops into a passage vortex. These vortical structures and their interaction (generally termed "secondary flows") are sources of aerodynamic loss in the cascade; furthermore, they sweep coolant from the endwall and increase endwall heat transfer coefficients.

Graziani et al. [4], Kang et al. [5], and Ames et al. [6] presented results of endwall heat transfer influenced by secondary flows. Measurements of heat transfer coefficients indicated regions of high heat transfer at the blade leading edge, and adjacent to the suction side of the airfoil downstream of the passage throat. All of the investigators attributed the high heat transfer coefficients to the effects of the horseshoe and passage vortices. Goldstein and Spores [3] used naphthalene mass transfer to infer heat transfer coefficients and deduced the existence of additional corner vortices along the suction side of the vane.

Coolant leakage was investigated by Blair [7] who presented endwall heat transfer from flow through a two-dimensional slot upstream of a linear cascade. Measured endwall heat transfer coefficients were similar with and without the additional slot flow. However, measurements of adiabatic effectiveness over a range of blowing ratios revealed that coolant accumulated along the suction side of the vane in the passage. Granser and Schulenberg [8] and Knost and Thole [9] reported similar trends of coolant accumulation. Computational predictions by Knost and Thole [10] indicated that streamline paths near the endwall became increasingly more directed toward the pressure side of the vane passage as flow rates increased through their upstream slot configuration.

Studies have been completed with upstream leakage in a contoured endwall vane cascade, where the contour serves to accelerate the flow and thin the boundary layer with the aim of reducing secondary flows. Burd et al. [11] found that coolant effectiveness levels and coolant coverage were increased for higher coolant ejection rates from an upstream flush slot on their contoured endwall. They conjectured that the momentum of the slot coolant at higher flow rates enabled it to avoid being entrained into the secondary flow vortices.

The only known study of thermal expansion of the combustor-turbine gap in the axial direction is Cardwell et al. [12]. Cardwell et al. found that adiabatic cooling effectiveness

coverage area was a function of slot momentum flux ratio, but effectiveness levels were dependent on the slot mass flow ratio.

The axial location of an upstream slot has also been shown to be important in the interaction of slot flow with secondary vortices. Kost and Nicklas [13] and Nicklas [14] presented aerodynamic and heat transfer measurements for upstream slot and passage discrete hole film cooling in a transonic cascade. For slot coolant ejection at 1.3% of the core flow rate and no passage film cooling, they found that the slot flow intensified the horseshoe vortex and increased heat transfer coefficients by nearly three times that of no slot flow. They attributed this dramatic increase to the fact that their slot, at $0.2C_{ax}$ upstream of the vane, was intensifying the horseshoe vortex by injecting at the separation location on the endwall. Kost and Mullaert [15] studied the same airfoil geometry, but moved the flush slot to $0.3C_{ax}$ upstream of the vane. They found that for this configuration, slot flow stayed closer to the endwall and provided better cooling than flow from the slot located at $0.2C_{ax}$ upstream of the vane.

The study reported in our paper expands upon the work of Cardwell et al. [12] by including heat transfer coefficient and shear stress measurements. It is also important to note that the slot locations relative to the vane differ between this study and that of Cardwell et al. [12], which will be addressed.

## Experimental Facility and Methodology

Endwall friction coefficients, adiabatic effectiveness, and heat transfer coefficients were measured in a closed-loop, low-speed wind tunnel, depicted in Figure 1.1 and previously described by Cardwell et al. [12]. The flow was driven by a 50-hp axial fan, and passed through a heat exchanger. A porous plate with 25% open area diverted flow into the secondary path from the primary flow path. Note that the tunnel has upper and lower secondary flow paths; only the top secondary flow path was used in this study. For adiabatic effectiveness measurements, the primary path was heated with a 55kW electrical resistance heater bank to increase the flow temperature to 45°C. The secondary path was further cooled with a heat exchanger to 20°C to increase the temperature differential between the mainstream and coolant leakage flow. To measure the convective heat transfer coefficients, the coolant and mainstream temperatures were matched with no primary flow heating or additional secondary flow cooling needed.

Downstream of the heat exchanger shown in Figure 1.1, the primary flow next passed through several screens and a contraction section. The contraction, located 2.9 vane chords upstream of the vane, reduced the flow area from 1.11 $m^2$ to 0.62 $m^2$ through symmetric 45° bounding walls. The primary flow area remained constant up to the corner test section.

The corner test section contained two full nozzle guide vanes and a third partial vane connected to a flexible wall to maintain the desired pressure distribution along the center vane. The vane design was a three-dimensional extrusion of a two-dimensional midspan airfoil geometry. The vanes were scaled up by a factor of nine to allow for high measurement resolution. The vanes were manufactured from low-density closed cell polyurethane foam for low conductivity. A description of the turbine vane parameters is given in Table 1.1.

The boundary layer entering the cascade was measured at a location 0.63C upstream of the vane stagnation. Table 1.2 lists the turbulent inlet boundary layer parameters, which were maintained throughout this study. The measured inlet turbulence intensity and length scales were 0.7% and 4 cm (0.07C), respectively. Although the turbulence intensity is lower than that typically found in an engine, the effect of turbulence was considered to be of secondary interest and was not examined in this study.

To simulate the leakage interface between a combustor and a turbine, a two-dimensional slot was placed upstream of the turbine vane bottom endwall, as illustrated in Figure 1.2. This combustor-turbine interface gap was based on the geometry presented by Cardwell et al. [12], and will be referred to as an upstream slot in this paper. Cardwell et al. [12] based their upstream slot design on discussions with several industrial contacts. The primary difference in the slot geometry between our study and that of Cardwell et al. [12] is the location of the slot relative to the vane stagnation ($0.38C_{ax}$ for Cardwell et al. [12] compared to $0.77C_{ax}$ for this study). The much larger upstream placement of the slot for this study was necessary to accommodate other endwall-airfoil geometries.

Two upstream slot widths were chosen to model the combustor-turbine interface. The nominal metering width, at a scale that is nine times that of the engine, was 1.43 cm (0.024C) with a flow length-to-width ratio of 1.9. The contracted slot metering width was 50% of the nominal slot width, and will be referred to as the half slot. The distance of the slot centerline to the vane stagnation was maintained for both slot widths. Both slots had an injection angle of 45° relative to the endwall.

Coolant was extracted from the top secondary channel of the wind tunnel by a 2-hp blower and fed to a plenum located below the upstream slot. To calculate the average mass flow exiting the slot, the inviscid blowing ratio from the slot was multiplied by an assumed discharge coefficient of 0.6, which is the commonly-accepted value for flow from a sharp-edged orifice [16]. Note that the coolant-to-mainstream density ratio was fixed at 1.1 for all adiabatic cooling effectiveness measurements. The density ratio in this study is lower than that typically found in an engine; however, past film cooling research has indicated that jet behavior best scales with momentum flux ratio. The leakage mass flow ratios and nominal slot metering width for this study were selected based on input from industrial contacts, so the blowing and momentum flux ratios are expected to be representative of engine values. For the convective heat transfer coefficient measurements, the coolant was maintained to within 0.1°C of the mainstream temperature, resulting in a density ratio of 1.0. Table 1.3 lists the coolant settings investigated for this paper. Mass flow from the upstream slot is reported as a percentage of the mass flow entering a single vane passage.

*Endwall Friction Coefficient Measurements*

Endwall friction coefficient measurements were made using oil film interferometry; see the review by Naughton and Sheplak [17], and implementation of the method in linear cascades by Harrison [18] and Holley and Langston [19]. Oil film interferometry (OFI) is based upon the dynamic behavior of a thin oil film. OFI is similar in concept to oil flow visualization, except that the oil layer is extremely thin (on the order of visible light wavelengths), and the height of the oil film is quantified to enable calculation of wall friction coefficients. The equation used in this study to determine the friction coefficient is:

$$C_f = L \Big/ 2h_{oil} \int \frac{\rho U_{\infty,in}^2}{2\mu_{oil}} dt \tag{1.1}$$

To derive Eq. (1.1), a mass and momentum balance is performed on a differential control volume aligned with the endwall (limiting) streamline. The mass balance gives the height of the oil and its average convective velocity as functions of time and distance along the streamline. Based on an order-of-magnitude analysis for the oil film, the streamwise momentum can be simplified by recognizing that the Reynolds number for the oil film is much less than one (thus the inertial terms are negligible). Then, the momentum equation can be solved for the oil velocity (retaining the pressure gradient, gravity, and shear terms) by applying no-slip boundary

conditions at the wall-oil interface, and the desired shear at the air-oil interface. Combining the momentum and mass balance results yields the thin oil-film equation:

$$\frac{\partial h_{oil}}{\partial t} + \frac{\partial}{\partial s}\left( \frac{\tau_{w,s} h_{oil}^2}{2\mu_{oil}} - \frac{h_{oil}^3}{3\mu_{oil}} \left\{ \frac{\partial P}{\partial s} - \cancel{\rho_{oil} g_s} \right\} \right) = 0 \tag{1.2}$$

For representative values pertinent to this study ($h_{oil}$=1 μm, $\nu_{oil}$=100 cSt, $\tau_{w,s}$=10 Pa, $\rho_{oil}$=1000 kg/m$^3$, dP/ds=100 Pa/m, $g_s$=10 m/s$^2$), order-of-magnitude analysis on the terms in the parentheses of Eq. (1.2) shows that the shear stress term is at least two orders of magnitude larger than the other terms, which are then neglected. For spatially constant shear stress over the region of interest (reasonable assumptions in this study because of the large scale and small measurement sizes), the reduced oil film equation can be solved by separation of variables for the height of the oil in terms of the shear stress, distance along the streamline, and time. Note that the shear stress is non-dimensionalized by the inlet dynamic pressure before performing separation of variables, so that the dynamic pressure appears in the integral in Eq. (1.1). The solution requires measurement of the oil height only at the end of the wind tunnel run, since the conditions leading to the final oil film thickness are integrated over time.

Fizeau interferometry provides a means of measuring the height of the oil. Light strikes the surface of the oil film and is reflected and refracted. The phase difference (φ) between the initially reflected and refracted rays will attenuate or augment the rays, creating interference bands (fringes). The phase difference is related to the height of the oil by the wavelength of the light rays, the optical properties of air and oil, and the incident light angle:

$$h_{oil} = \frac{\lambda \varphi}{4\pi}\left( \frac{1}{\sqrt{n_{oil}^2 - n_{air}^2 \sin^2 \theta_i}} \right) \tag{1.3}$$

The phase difference between successive fringes is an integer multiple of 2π. The average spacing between successive fringes (L) is determined by a least-squares cosine fit to the pixel intensity profile of the fringe pattern [19] to determine the period of the intensity profile. The location of the friction coefficient measurement in the interferogram is taken as the center of the intensity profile.

To measure endwall friction coefficients in the cascade, small silicone oil droplets, nominally less than 5 mm in diameter, were placed on 0.05 mm thick rectangular sheets of nickel foil that had been adhered to the endwall (see Figure 1.3). For the entire endwall, three

viscosities of silicone oil (100 cSt, 500 cSt, and 1000 cSt) were used to maximize the range of the OFI method throughout the vane passage. The oil viscosity was corrected for temperature variation during a test (generally less than 4°C) by the correlation of Naughton and Sheplak [17]. The time history of the cascade inlet dynamic pressure and the flow temperature were recorded over the entirety of a test, which nominally took twenty minutes. The foil patches were carefully removed after a test and imaged in a fixture with a nearly monochromatic sodium vapor lamp ($\lambda$=589, 589.6 nm) to obtain the interferograms. Several tests were required to obtain over 400 data points on the endwall.

Shear stress vectors were obtained by examining the progression of features in the fringe pattern. For example, a notch in a fringe will propagate downstream in the direction of the limiting streamline. Note, however, that measurements were only obtained on the portion of a fringe that was undisturbed by dust particle wakes or upstream oil droplets.

The OFI method was benchmarked by measuring friction factors in fully developed flow in a square channel. Friction factor measurements agreed with textbook correlations to within 5% over a wide range of channel Reynolds numbers ($25{,}000 < Re_{Dh} < 45{,}000$).

The partial derivative method described by Moffat [20] was used to calculate uncertainties for the measurements of friction coefficients. Uncertainty was estimated as $\partial C_f = \pm 5.8\%$ for both low ($C_f$=0.004) and high ($C_f$=0.126) values of friction coefficients, and was dominated by uncertainty in the interferogram spacing.

*Adiabatic Effectiveness Measurements*

Adiabatic wall temperatures for endwall effectiveness of upstream slot coolant were obtained from infrared thermography measurements of the bottom endwall surface. The endwall was manufactured from a 2.54 cm thick sheet low-density closed-cell polyurethane foam, which has a low thermal conductivity (0.0287 W/m-K) to minimize conduction errors. The endwall was instrumented with type-E thermocouples throughout the vane passages for calibration of infrared thermography images. The endwall and thermocouples were painted with flat black paint, which has a nominal emissivity of 0.96 and enabled good resolution of surface temperatures with the infrared camera. Infrared-reflective finishing nails were used as image transformation markers.

An infrared camera was used to capture spatially-resolved surface temperatures on the bottom endwall. Based on an uncertainty analysis, five images were taken at each location and

averaged, where each image is also an average of 16 frames taken by the camera. The camera's spatial integration was approximately 0.17 mm (0.0012C). Images were post-calibrated by determining the emissivity and background temperature of the image through matching of the image temperatures with the acquired thermocouple measurements. The thermocouples and the calibrated images generally agreed to within 0.3°C. An in-house MATLAB routine was developed to assemble the individual images into a single endwall map.

A one-dimensional correction for endwall conduction effects was applied to all adiabatic effectiveness measurements. The resulting $\eta$ correction was 0.14 at $\eta$=0.75 measured downstream of the slot, and 0.05 for $\eta$=0.07 measured at the exit of the vane passage.

The partial derivative method was used to calculate uncertainties for the measurements of adiabatic cooling effectiveness. For adiabatic surface temperatures, a precision uncertainty of ±0.33°C was determined by taking the standard deviation of six measurement sets of IR camera images, with each set consisting of five images. Since the IR images were calibrated as closely as possible to the thermocouples in each image, the bias uncertainty for an image was assumed to be the root-sum-square of the thermocouple bias uncertainty (±0.2°C) and the average deviation of the calibrated images from the thermocouples (±0.34°C). In this way, a bias uncertainty of ±0.39°C was determined. Using the bias and precision uncertainties, a total uncertainty of ±0.51°C was estimated for the IR surface temperature measurements. Overall uncertainty in adiabatic effectiveness was calculated to be $\partial\eta$=±0.036 at a $\eta$ value of 0.1, and $\partial\eta$=±0.026 at a $\eta$ value of 0.8.

*Heat Transfer Measurements*

Endwall heat transfer measurements were taken by imaging surface temperatures on a constant heat flux plate attached to a 2.54 cm thick sheet of the closed-cell polyurethane foam. The heat flux plate consisted of a 37 μm copper layer on top of a 75 μm thick kapton layer, in which 25 μm inconel elements were embedded in a serpentine pattern. The heater covered the entire endwall, from immediately downstream of the slot to 0.3C downstream of the vane trailing edge, as shown in Figure 1.2. E-type thermocouples, embedded in the foam endwall, were placed in thermal contact with the bottom surface of the heater by thermal cement. A conduction bias between the bottom-mounted thermocouple and the infrared top-surface measurement was accounted for by a one-dimensional calculation of the thermal resistance of the heater. The infrared camera was also used to capture surface temperatures on the heat flux plate.

The input heat flux to the endwall was calculated by measuring the voltage across the heater circuit, as well as the voltage across a precision resistor (1Ω) in series with the circuit, which gave the current. This flux was corrected for conduction and radiation losses, which accounted for a maximum of 0.2% and 21% of the input power, respectively. Note that the conduction and radiation corrections varied locally with the highest correction occurring at the highest surface temperatures. Uncertainty in Stanton numbers was dominated by the uncertainty in surface temperature measurements. For those measurements, a precision uncertainty of ±0.22°C was estimated from the standard deviation of six IR image measurement sets, and a bias uncertainty of ±0.88°C was determined in the same way as for the adiabatic effectiveness measurements. Overall uncertainty in Stanton numbers was $\partial St=\pm 0.00011$ (3.3%) at a St value of 0.003, and $\partial St=\pm 0.0009$ (7.5%) at a St value of 0.011.

## Discussion of Results

Endwall friction coefficient measurements without any upstream slot flow over the endwall will be presented first, followed by adiabatic cooling effectiveness results with upstream slot flow. Heat transfer coefficient measurements with and without upstream slot flow are then discussed. Finally, the net heat flux reduction parameter, which incorporates both heat transfer coefficients and adiabatic cooling effectiveness, is presented.

### *Friction Coefficients without an Upstream Slot*

Oil film interferometry (OFI) measurements of endwall friction coefficients were linearly interpolated to a uniform grid, and then downsampled to create the vector plot in Figure 1.4. Several unique features due to secondary flow are visible in the vector field. Shear decreases as flow approaches the vane leading edge and begins to stagnate. A saddle point is also visible upstream of the vane, where flow diverges around the leading edge. The saddle point is the intersection of flow attachment and separation lines on the endwall. At the separation line, the incoming boundary layer separates from the endwall and rolls up into the horseshoe vortex. The vortex roll-up causes flow to wash down the airfoil toward the endwall and then move upstream, away from the airfoil-endwall junction.

Further in the passage, cross-passage flow from the passage vortex sweeps from the pressure side of the lower airfoil to the suction side on the adjacent airfoil. Because of this, the exit turning angle of the airflow near the endwall is much larger than the exit turning angle of

inviscid flow away from the wall. The measured friction coefficient magnitudes near the passage throat have increased relative to the inlet values, resulting from the flow acceleration in the vane passage.

Figure 1.5 shows a prediction of inviscid streamlines near the mid-span of the vane using FLUENT 6.2 [21], which are superimposed upon the endwall streamlines computed from the friction coefficient measurements. The endwall streamlines are representative of the flow streamlines in the limit as the wall is approached, and thus are also known as limiting streamlines. Figure 1.5 shows the endwall separation line also computed from the endwall friction coefficient vector measurements. The separation line was obtained by computing multiple streamline paths starting very near to the saddle point, and taking the mean of the paths. Note that since the saddle point is a location of zero shear stress, its exact location could not be found since the OFI method requires some detectable amount of oil flow.

*Adiabatic Effectiveness Levels from an Upstream Slot*

Contours of adiabatic cooling effectiveness for upstream slot flow at various flow rates and metering widths are presented in Figure 1.6. Note that for all cases in this study, there is a hot region around the vane-endwall junction where slot coolant is not present. This pattern is caused by the roll-up of the horseshoe vortex at the vane leading edge, which brings hot mainstream gases down to the endwall, and sweeps coolant off of the endwall. Further downstream, the combination of the horseshoe and passage vortices entrains coolant and sweeps it to the suction side of the vane.

To visualize endwall results in a more quantitative sense, values were extracted from the endwall data along the paths of inviscid streamlines obtained from a CFD prediction of the vane flowfield with FLUENT 6.2 [21]. Streamlines were released at mid-span of the vane from three pitch locations, corresponding to Y/P = 0.25, 0.50 and 0.75 as shown in Figure 1.6a. These streamlines are denoted as 0.25P, 0.50P, and 0.75P, respectively. Figure 1.7 presents the adiabatic effectiveness levels on the endwall resulting from the upstream slot flow, along each of the three streamline paths. The abscissa of the plots is non-dimensionalized distance along the streamline, shifted so that s/C=0 corresponds to where the streamline would cross an imaginary pitchwise line connecting adjacent vane stagnation points. Note that the plots in Figure 1.7 have different abscissas, since the streamlines have different lengths through the vane passage. In the shifted streamline coordinate system, the upstream slot is located at s/C=-0.35. Data is not

plotted directly downstream of the slot, but rather starting at s/C=-0.3, in order to avoid the high measurement uncertainty at the start of the thermal boundary layer in the heat transfer coefficient measurements.

In Figure 1.7, effectiveness values eventually become zero as each streamline path crosses into the hot region. Note that in most cases, the path of the 0.75P streamline crosses the hot ring region around the suction side of the vane, passes through the narrow band of coolant being swept to the suction side by the passage vortex, and re-enters the pressure side hot region (refer to Figure 1.6a). These crossings explain why effectiveness along the 0.75P path decays, increases, and then progressively decays.

As described earlier, the slot in this study was positioned at $0.77C_{ax}$ upstream of the vane stagnation. A slot located far upstream, away from the influence of the vane, can reduce or eliminate the potential for hot gas path ingestion into the slot, but from a practical point of view may be difficult to implement in an engine. The effect of moving the slot upstream is shown in Figure 1.8. A similar lack of coolant coverage around the base of the vane is seen between this study's results and those of Knost and Thole [10], for 1% slot flow from a nominal slot. The horseshoe and passage vortices control the distribution of coolant in the passage, despite the differences in slot location. Note that the upstream slot for the case in Figure 1.8 had the same geometry as the slot tested by Knost and Thole [10], but Knost and Thole positioned their slot at $0.38C_{ax}$ from the vane leading edge. In the contours of Figure 1.8, and along the inviscid streamline paths in Figure 1.7, Knost and Thole's [10] slot blowing at 1.0% MFR exhibits higher local effectiveness than the nominal slot blowing at 1.0% MFR. Coolant ejected farther upstream interacts more with the mainstream and thus is less effective when it reaches the vane passage. However, the slot in Knost and Thole's [10] study also results in more poorly distributed effectiveness levels across the endwall than for a slot ejecting farther upstream (see Figure 1.8). High effectiveness gradients would be a durability concern since they could lead to large gradients in endwall metal temperature and increased thermal stresses.

The effect of increasing the coolant flow rate can be seen by comparing the contours in Figures 1.6a and 1.6c for the nominal slot at two coolant flow rates, as well as in Figures 1.6b and 1.6d for the half slot at two coolant flow rates. For a given upstream slot width, effectiveness levels from upstream slot coolant over the endwall increase with increasing slot mass flow rates. Also, coolant coverage is more uniform downstream of the slot and is better able to penetrate

into the hot ring around the vane-endwall junction for a slot MFR of 1% as compared to a slot MFR of 0.5%. Figures 1.7a and 1.7b show that for a given upstream slot width, the location of zero effectiveness along the 0.25P and 0.50P inviscid streamline paths moves farther downstream (convects farther into the passage) as the slot mass flow rate is increased from 0.5% to 1.0%.

Matching the upstream slot leakage flow while decreasing the slot width increases the coolant momentum, with the effect of increasing overall coolant coverage in the passage. Comparison of Figure 1.6a with 1.6b for the same mass flux ratios with differing slot widths (differing momentum flux ratios), and Figure 1.6c with 1.6d also for the same mass flux ratios with differing slot widths, shows that the half slot at a given mass flow rate produces more uniform coolant coverage upstream and around the vane-endwall junction than the nominal slot at the same mass flow rate. Along the streamline paths in Figure 1.7, for a given mass flow rate, coolant from the half slot generally has higher levels of effectiveness than the nominal slot as the coolant enters the vane passage (downstream of s/C=0). Maintaining the mass flow rate from the slot, while decreasing the metering area of the slot, requires a larger plenum-to-freestream pressure differential which forces coolant out of the slot more evenly. This finding is in agreement with the conclusions of Cardwell et al. [12], even though the upstream slot in this study was located farther upstream of the vane leading edge than in Cardwell et al.

The effect of matching the slot momentum flux ratio for the nominal and half slot is perhaps a more realistic situation for a turbine engine. Generally, the coolant will be supplied at a constant pressure relative to the mainstream. The effect of reducing the upstream slot width will be to reduce the coolant mass flow rate, but the average momentum flux ratio will remain the same. The coolant coverage region in Figure 1.6b for the half width slot at a MFR of 0.5% appears similar to the coverage region from the nominal slot at the same momentum flux ratio (Figure 1.6c). However, coolant effectiveness levels from the half slot flow are lower relative to the nominal slot at the same momentum flux ratio, since the nominal slot is ejecting more coolant.

When the endwall separation line for no upstream blowing is overlaid on the adiabatic cooling effectiveness contours in Figure 1.6a and 1.6d, it is apparent that for low slot coolant momentum, the trajectory of the coolant is dictated by the secondary flow vortices. For the highest momentum flux ratio tested, however, some coolant penetrates downstream of the

separation line, indicating that the coolant has a more significant interaction with endwall secondary flow in this case.

*Heat Transfer Coefficients for an Upstream Slot*

Endwall heat transfer coefficients were measured with and without an upstream slot flow. For the baseline with no slot flow, a qualitative comparison was made to Kang et al. [5], who used the same airfoil geometry. Similar results were achieved, as can be seen in Figures 1.9a and 1.9b for both baselines with no slot flow, despite differences in the upstream tunnel geometry and inlet boundary layer thicknesses ($\delta/S = 0.09$ for Kang et al. [5] and $\delta/S = 0.18$ for our work). High heat transfer coefficients are seen in Figures 1.9a and 1.9b near the vane stagnation region resulting from the horseshoe vortex. The effects of the passage vortex are seen further downstream as the contours sweep to the suction surface.

Figures 1.9b through 1.9f compare heat transfer coefficients with and without upstream slot flow for the various slot widths and flow rates. The overall effect of injection along the endwall is that the heat transfer coefficients are slightly increased in the cases with injection, relative to the baseline without injection. Figure 1.10 shows endwall heat transfer augmentation levels relative to the no leakage flow case along the 0.25P, 0.50P, and 0.75P streamline paths. Note that overall, augmentation levels with upstream slot blowing indicate higher heat transfer throughout most of the passage.

The effect of increasing the slot mass flow rate, while maintaining the slot width, is illustrated for the nominal slot in Figures 1.9c and 1.9e and for the half slot in Figures 1.9d and 1.9f. Stanton numbers increase slightly throughout the passage when the slot mass flow rate is increased from 0.5% to 1.0% for a given slot width. Heat transfer augmentation levels along the inviscid streamline paths (Figure 1.10) are generally higher as the mass flow rate increases through a given slot width. An exception to this trend, however, is the region around s/C=-0.05 on the 0.25P streamline path (Figure 1.10a) and the region around s/C=0.10 on the 0.50P streamline path (Figure 1.10b). At these locations, there is no difference in heat transfer augmentation for the nominal slot injecting coolant at either mass flow rate. It was noted that the 0.25P streamline path crosses the separation line for no upstream slot blowing at s/C=-0.07, while the 0.50P streamline path crosses the separation line at s/C=0.11 (refer to Figure 1.9c). These results indicate that the separated flow dictates the heat transfer augmentation near the endwall separation line, rather than the injection itself. However, for the half slot, increasing its

mass flow from 0.5% to 1.0% increases the coolant momentum to the point that the injection begins to interfere with the horseshoe vortex.

As mentioned earlier, for a turbine engine, a decrease in upstream slot width would result in a decrease in slot mass flow rate, but nominally the same momentum flux ratio. The effect of decreasing the slot width while maintaining the same momentum flux is seen by comparing the contours of Figures 1.9d and 1.9e. Stanton numbers are slightly lower for the half slot at a MFR of 0.5%, compared to the nominal slot at a MFR of 1.0%, even though both have the same momentum flux.

The endwall separation line, deduced from the measured friction coefficients with no upstream slot blowing, is overlaid on the heat transfer coefficient results for no upstream slot blowing (Figure 1.9b), and for blowing at the lowest and highest momentum flux ratios in Figures 1.9c and 1.9f, respectively. There is a region of low heat transfer between the vanes near the passage entrance that persists farther downstream for the case with the highest momentum flux ratio (Figure 1.9f) relative to the lowest momentum flux ratio (Figure 1.9c). These behaviors suggest that the upstream slot injection at a high momentum flux ratio reduces horseshoe vortex strength.

*Net Heat Flux Reduction for an Upstream Slot*

The determination of convective heat transfer to a turbine endwall with film-cooling requires knowledge of the film heat transfer coefficient, the metal wall temperature, and the adiabatic wall (recovery) temperature. The addition of coolant to the endwall reduces the adiabatic wall temperature and thus the driving potential for heat transfer. The mixing and flow disturbance induced by the coolant injection, however, generally increases the convective heat transfer coefficients. The net heat flux reduction parameter (NHFR) incorporates the effects of convective heat transfer coefficients and coolant effectiveness on the overall augmentation to the heat load to the component. To deduce the net heat flux reduction parameter, the component wall metal temperature must also be known, since it is the other driving temperature for heat transfer into the part. The non-dimensional form (denoted as $\varphi$) relates the wall temperature to the freestream and coolant temperatures. Since the wall temperature is dependent on the vane metal conductivity and internal cooling scheme, it had to be assumed for this study, which used adiabatic materials for the endwall. A value of $\varphi = 1.6$ was assumed based on typical film-

cooled engine conditions (Sen et al. [22]). Note that values of NHFR < 0 indicate that the film cooling scheme is causing an increase in the overall heat flux experienced by the surface.

Figure 1.11 presents the NHFR calculated along each of the inviscid streamline paths. For the cases that have been studied, it is clear that there is a strong benefit of the leakage coolant at the entrance to the vane passage. Downstream, however, the cooling benefit of the leakage flow produces a detrimental effect where no coolant is present but the heat transfer coefficients have been increased. This increase is caused by alterations to the secondary flows that in turn increase the overall convective heat transfer coefficients. The 0.25P and 0.50P streamline paths, shown in Figures 1.11a and 1.11b, respectively, indicate that the addition of upstream slot flow at any mass flow rate or slot width causes NHFR values that are less than zero near the exit of the vane passage. The lack of coolant penetration into the hot ring around the vane, combined with slight heat transfer coefficient augmentations from slot flow, leads to an increased net heat flux that would be experienced by the part.

It is apparent that the trends of NHFR along the streamline paths in Figure 1.11 parallel the trends of the effectiveness levels, and many of the same conclusions about the effects of slot flow can be made. Although increasing the slot flow rate tends to increase heat transfer coefficients, the additional coolant from a given slot width at 1.0% MFR relative to 0.5% MFR results in a net heat flux reduction. Also, the better coolant coverage from a half-width slot at a given mass flow rate reduces net heat flux, as compared to the nominal slot at the same mass flow rate. Finally, the case of matched momentum flux ratios for the nominal and half slots shows that, despite reduced Stanton number augmentations from the half slot blowing versus the nominal slot blowing, the lower amount of coolant ejected from the half slot at a MFR of 0.5% is not as effective in reducing heat flux into the endwall as is the coolant from the nominal slot at a MFR of 1.0%.

An overall, area-averaged NHFR is shown in Figure 1.12 as a function of slot momentum flux ratio. Coolant ejection from the half slot does a better job in decreasing average heat flux into the endwall than coolant from the nominal slot, when both are ejecting coolant at a given mass flow ratio. However, blowing from the half slot at a momentum flux ratio of 0.13 (MFR=0.5%) increases the average net heat flux (decreases NHFR parameter) by 26%, compared to the nominal slot blowing at the same momentum flux ratio (I=0.13, MFR=1.0%).

Thus, axial contraction of the upstream slot, in a situation where the slot momentum flux is maintained, would increase endwall heat transfer.

## Conclusions

Measurements of adiabatic cooling effectiveness and heat transfer coefficients on the endwall, from leakage flow through a two-dimensional upstream slot representing a combustor-turbine interface gap, were presented. Two slot flow rates and two slot widths were tested, to determine the effect of the contraction of the slot on the endwall heat transfer.

The dominance of the endwall secondary flow on upstream slot coolant coverage was demonstrated by moving the slot further upstream. The coverage area of the slot coolant, when the slot was located $0.77C_{ax}$ upstream of the vane, was similar to the coverage area for a slot located $0.38C_{ax}$ upstream. It was noted, however, that effectiveness levels in the passage were lower for the slot placed farther upstream since the coolant had more distance to interact with the mainstream flow.

For a fixed slot width, increasing the slot mass flow resulted in slightly increased heat transfer coefficients, but also higher adiabatic cooling effectiveness levels. Coolant exited the slot more uniformly at the higher slot flow rates, since the higher flow rate required an increase in slot pressure ratio. Overall, the net heat flux to the endwall was reduced, since more coolant was present at the higher flow rates.

Decreasing the slot width while maintaining a constant slot mass flow resulted in larger coolant coverage areas and increased local effectiveness levels. Moreover, heat transfer coefficient augmentations from the half width slot were lower than augmentations from the nominal slot. Area-averaged values of the net heat flux reduction parameter indicated that the coolant from the half slot width reduced the net heat flux to the endwall compared to the nominal slot, when both were ejecting coolant at the same mass flow rate. The higher momentum of slot coolant from the half width slot enabled it to penetrate farther into the passage.

Overlaying the endwall separation line for no blowing on contours of effectiveness and heat transfer coefficients revealed that for low slot momentum, the endwall secondary flow dictated the coolant trajectory in the passage. At the highest momentum flux ratio tested, a significant amount of coolant penetrated downstream of the endwall separation line, and heat

transfer coefficients were reduced compared to the low momentum slot flow. The high coolant momentum in this case is suspected to have reduced the horseshoe vortex strength.

These results indicate that leakage flow through the combustor-turbine interface can provide cooling to the endwall, with a more uniform distribution of coolant when the interface is placed farther upstream. More uniform coverage reduces the spatial temperature variation in the turbine endwall metal, which is beneficial for durability. The effects of thermal expansion of the interface, however, need to be carefully considered since higher heat loads can result when the combustor-turbine interface gap contracts. Understanding how a leakage interface expansion impacts the heat transfer and cooling effectiveness of the leakage flow may help a designer to protect the part during unwanted thermal expansion incidents with the least amount of coolant.

## Acknowledgments

The authors would like to thank the National Science Foundation's GOALI program for funding this research (Grant No. 0412971). We would also like to acknowledge our partners in the GOALI program: Joel Wagner and Peter Tay (Pratt & Whitney), and Dr. Lee Langston and Brian Holley (University of Connecticut).

## Nomenclature

| | |
|---|---|
| $C$ | true chord of stator vane |
| $C_{ax}$ | axial chord of stator vane |
| $C_f$ | friction coefficient, see Eq. (1.1) |
| $C_p$ | heat capacity at constant pressure |
| $g$ | gravitational acceleration (9.81 m/s$^2$) |
| $h$ | heat transfer coefficient |
| $h_{oil}$ | height of oil film |
| $I$ | average momentum flux ratio, $I = \rho_c U_c^2 / \rho_\infty U_{\infty,in}^2$ |
| $L$ | spacing between oil film interferogram bands (fringes) |
| $M$ | average blowing ratio, $M = \rho_c U_c / \rho_\infty U_{\infty,in}$ |
| $MFR$ | mass flow ratio, $MFR = \dot{m}_c / \dot{m}_{in}$ |
| $n$ | index of refraction |
| $NHFR$ | net heat flux reduction, $NHFR = 1 - (h_f / h_0)(1 - \eta\varphi)$ |
| $\overline{NHFR}$ | area-averaged net heat flux reduction |
| $P$ | pitch of stator vane, or pressure |
| $Re_{Dh}$ | Reynolds number based on hydraulic diameter |
| $Re_{in}$ | inlet Reynolds number, $Re_{in} = CU_{\infty,in} / \nu$ |

| | |
|---|---|
| $Re_\theta$ | momentum thickness Reynolds number, defined as $Re_\theta = \theta U_{\infty,in} / \nu$ |
| s | distance along a streamline |
| S | span of stator vane |
| St | Stanton number, $St = h / \rho C_p U_{\infty,in}$ |
| t | time |
| T | temperature |
| U | axial velocity |
| X, Y, Z | vane coordinates, where X is turbine axial direction |

*Greek*

| | |
|---|---|
| $\delta$ | boundary layer thickness |
| $\eta$ | adiabatic effectiveness, $\eta = (T_\infty - T_{aw})/(T_\infty - T_c)$ |
| $\theta$ | momentum thickness |
| $\theta_i$ | incident light angle |
| $\lambda$ | light wavelength of sodium vapor lamp |
| $\mu_{oil}$ | dynamic viscosity of oil |
| $\nu$ | kinematic viscosity |
| $\rho$ | density |
| $\tau_w$ | wall shear stress |
| $\varphi$ | phase difference of light rays, or non-dimensional vane metal temperature, $\varphi = (T_\infty - T_c)/(T_\infty - T_w)$ |

*Subscripts*

| | |
|---|---|
| 0 | baseline conditions (no blowing) |
| aw | adiabatic wall |
| c | coolant conditions |
| in | inlet conditions |
| s | streamline coordinate |
| w | conductive (metal) wall |
| $\infty$ | local freestream conditions |

## References


[1] Langston, L.S., 1980, "Crossflows in a Turbine Passage," *J of Engineering for Power*, Vol. 102, pp. 866-874.

[2] Sharma, O.P. and Butler, T.L., 1987, "Predictions of Endwall Losses and Secondary Flows in Axial Flow Turbine Cascades," *J of Turbomachinery*, Vol. 109, pp. 229-236.

[3] Goldstein, R.J. and Spores, R.A., 1988, "Turbulent Transport on the Endwall in the Region Between Adjacent Turbine Blades," *J of Heat Transfer*, Vol. 110, pp. 862-869.

[4] Graziani, R.A., Blair, M.F., Taylor, J.R. and Mayle, R.E., 1980, "An Experimental Study of Endwall and Airfoil Surface Heat Transfer in a Large Scale Turbine Blade Cascade," *J of Engineering for Power*, Vol. 102, pp. 257-267.

[5] Kang, M., Kohli, A., and Thole, K.A., 1999, "Heat Transfer and Flowfield Measurements in the Leading Edge Region of a Stator Vane Endwall," *J of Turbomachinery*, Vol. 121, pp. 558-568.

[6] Ames, F.E., Barbot, P.A., and Wang, C., 2003, "Effects of Aeroderivative Combustor Turbulence on Endwall Heat Transfer Distributions Acquired in a Linear Vane Cascade," *J of Turbomachinery*, Vol. 125, pp. 210-220.

[7] Blair, M.F., 1974, "An Experimental Study of Heat Transfer and Film Cooling on Large-Scale Turbine Endwalls," *J of Heat Transfer*, pp. 524-529.

[8] Granser, D., and Schulenberg, T., 1990, "Prediction and Measurement of Film Cooling Effectiveness for a First-Stage Turbine Vane Shroud," 90-GT-95.

[9] Knost, D. G., and Thole, K. A., 2004, "Adiabatic Effectiveness Measurements of Endwall Film-Cooling for a First Stage Vane," GT2004-53326.

[10] Knost, D. G., and Thole, K. A., 2005, "Adiabatic Effectiveness Measurements of Endwall Film-Cooling for a First Stage Vane," *J of Turbomachinery*, Vol. 127, pp. 297-305.

[11] Burd, S.W., Satterness, C.J., and Simon, T.W., 2000, "Effects of Slot Bleed Injection Over a Contoured Endwall On Nozzle Guide Vane Cooling Performance: Part II - Thermal Measurements," 2000-GT-200.

[12] Cardwell, N.D., Sundaram, N., and Thole, K.A., 2006, "The Effects of Varying the

Combustor-Turbine Gap," GT2006-90089.

[13] Kost, F. and Nicklas, M., 2001, "Film-Cooled Turbine Endwall in a Transonic Flow Field: Part I-Aerodynamic Measurements," *J of Turbomachinery*, Vol. 123, pp. 709-719.

[14] Nicklas, M., 2001, "Film-Cooled Turbine Endwall in a Transonic Flow Field: Part II-Heat Transfer and Film-Cooling Effectiveness," *J of Turbomachinery*, Vol. 123, pp. 720-729.

[15] Kost, F. and Mullaert, A., 2006, "Migration of Film-Coolant from Slot and Hole Ejection at a Turbine Vane Endwall," GT2006-90355.

[16] Munson, B. R., Young, D. F., and Okiishi, T. H., 2002, *Fundamentals of Fluid Mechanics* (4th ed.), New York: John Wiley & Sons, Inc., p. 514.

[17] Naughton, J.W. and Sheplak, M., 2002, "Modern developments in shear stress measurement," *Progress in Aerospace Sciences*, Vol. 38, pp. 515-570.

[18] Harrison, S., 1990, "Secondary Loss Generation in a Linear Cascade of High-Turning Turbine Blades," *J of Turbomachinery*, Vol. 112, pp. 618-624.

[19] Holley, B., and Langston, L.S., "Surface Shear Stress and Pressure Measurements in a Turbine Cascade," GT2006-90580.

[20] Moffat, R. J., 1988, "Describing the Uncertainties in Experimental Results," *Experimental Thermal and Fluid Science*, Vol. 1, pp. 3-17.

[21] FLUENT (version 6.2.1), Fluent Inc., Lebanon, NH.

[22] Sen, B., Schmidt, D.L., and Bogard, D.G., 1996, "Film Cooling with Compound Angle Holes: Heat Transfer," *J of Turbomachinery*, Vol. 118, pp. 800-806.

**Table 1.1 Vane Geometry and Flow Conditions**

| | |
|---|---|
| Scaling factor | 9 |
| Scaled vane chord (C) | 59.4 cm |
| Axial chord/chord ($C_{ax}$/C) | 0.48 |
| Pitch/chord (P/C) | 0.77 |
| Span/chord (S/C) | 0.93 |
| Inlet Reynolds number ($Re_{in}$) | $2.2x10^5$ |
| Inlet mainstream velocity ($U_{\infty,in}$) | 6.3 m/s |
| Inlet, exit angle | 0°, 78° |
| Inlet, exit Mach number | 0.017, 0.085 |

**Table 1.2 Inlet Boundary Layer Characteristics**

| | |
|---|---|
| Boundary layer thickness/span (δ/S) | 0.18 |
| Displacement thickness/span (δ*/S) | 0.025 |
| Momentum thickness/span (θ/S) | 0.020 |
| Shape factor (δ*/θ) | 1.26 |
| Momentum thickness Reynolds number ($Re_\theta$) | 4138 |

**Table 1.3 Slot Coolant Settings**

| | **MFR** | **M** | **I** |
|---|---|---|---|
| Nominal slot width | 1.0% | 0.36 | 0.13 |
| | 0.5% | 0.19 | 0.03 |
| Half slot width | 1.0% | 0.73 | 0.50 |
| | 0.5% | 0.36 | 0.13 |

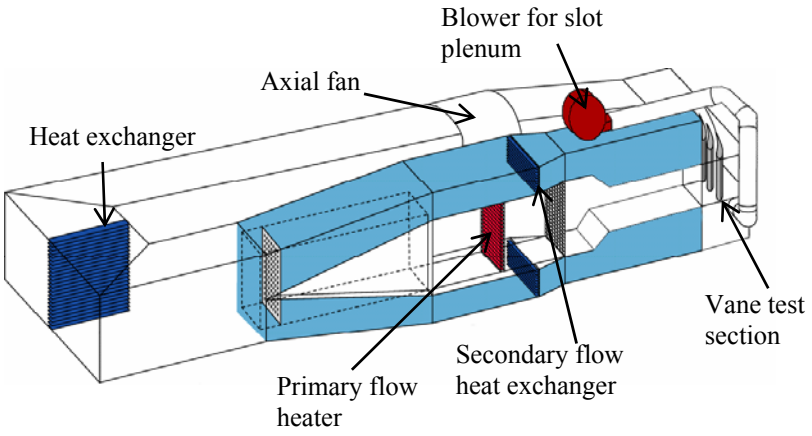


**Figure 1.1** **Large low-speed wind tunnel with separate flow conditioning paths and corner test section.**

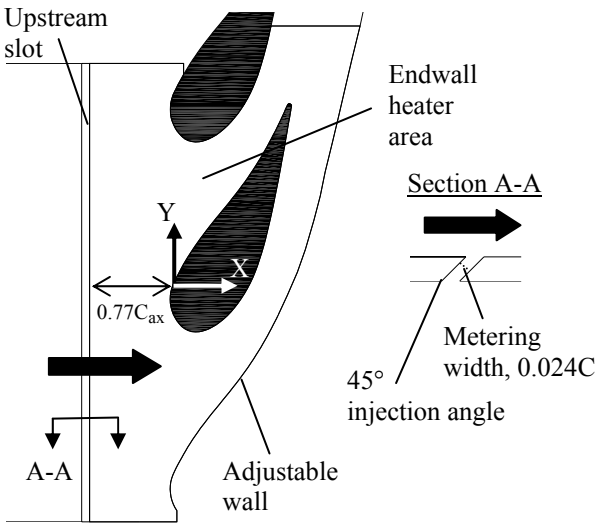


**Figure 1.2** **A schematic of the endwall and the combustor-turbine leakage interface (upstream slot) modeled in this study.**

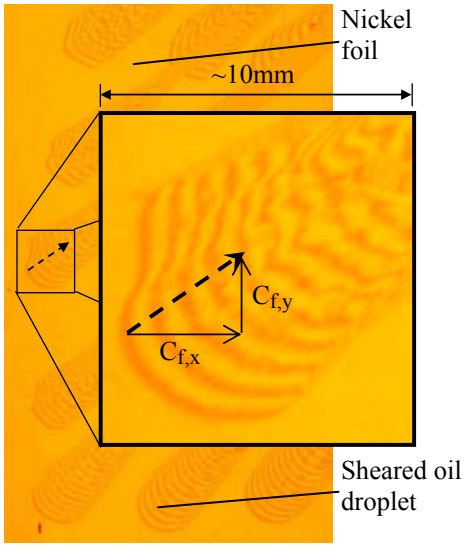


**Figure 1.3** **Example of oil film interferograms on nickel foil, used to determine endwall friction coefficient magnitude and direction.**

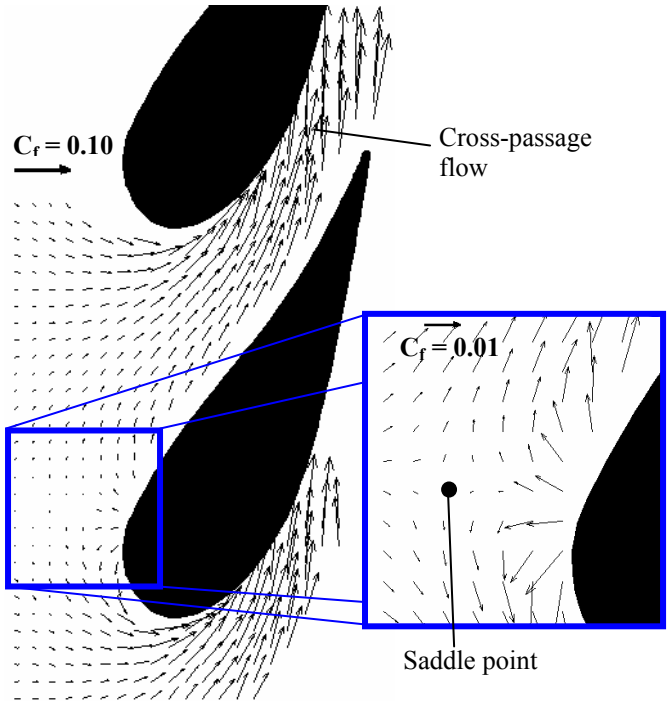


**Figure 1.4** **Measured friction coefficient vectors for no upstream slot flow, which illustrate the features of secondary flow over the endwall.**

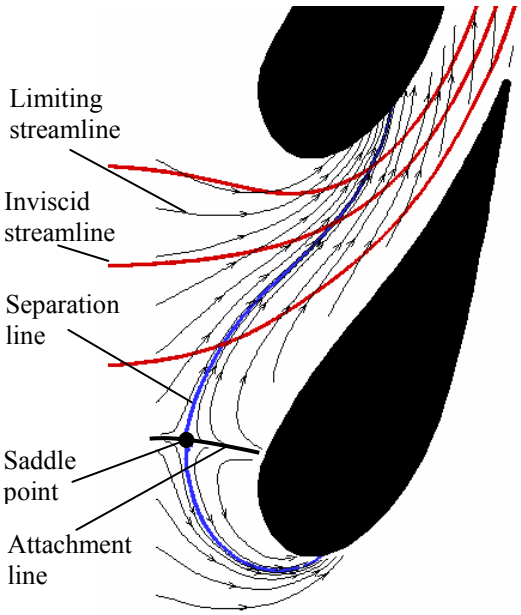


**Figure 1.5** **Endwall limiting streamlines and the separation line (blue) calculated from the friction coefficient vectors in Figure 1.4, with inviscid streamlines (red) from FLUENT [21] overlaid.**

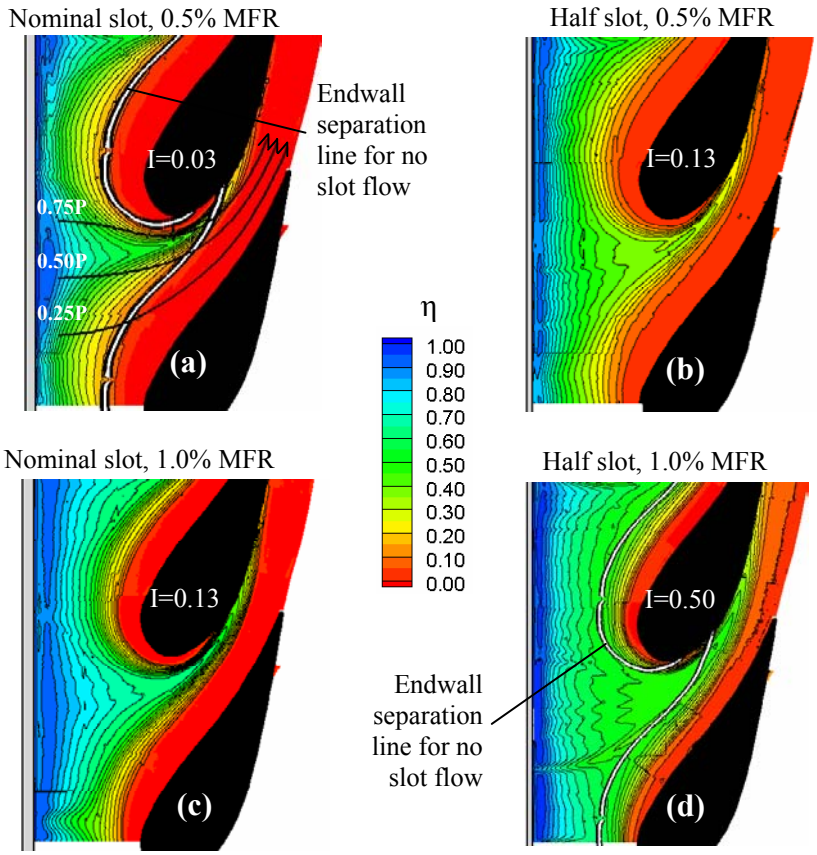


**Figure 1.6** **Contours of endwall effectiveness from upstream slot flow for (a) nominal slot, MFR=0.5%; (b) half slot, MFR=0.5%; (c) nominal slot, MFR=1.0%; (d) half slot, MFR=1.0%.**

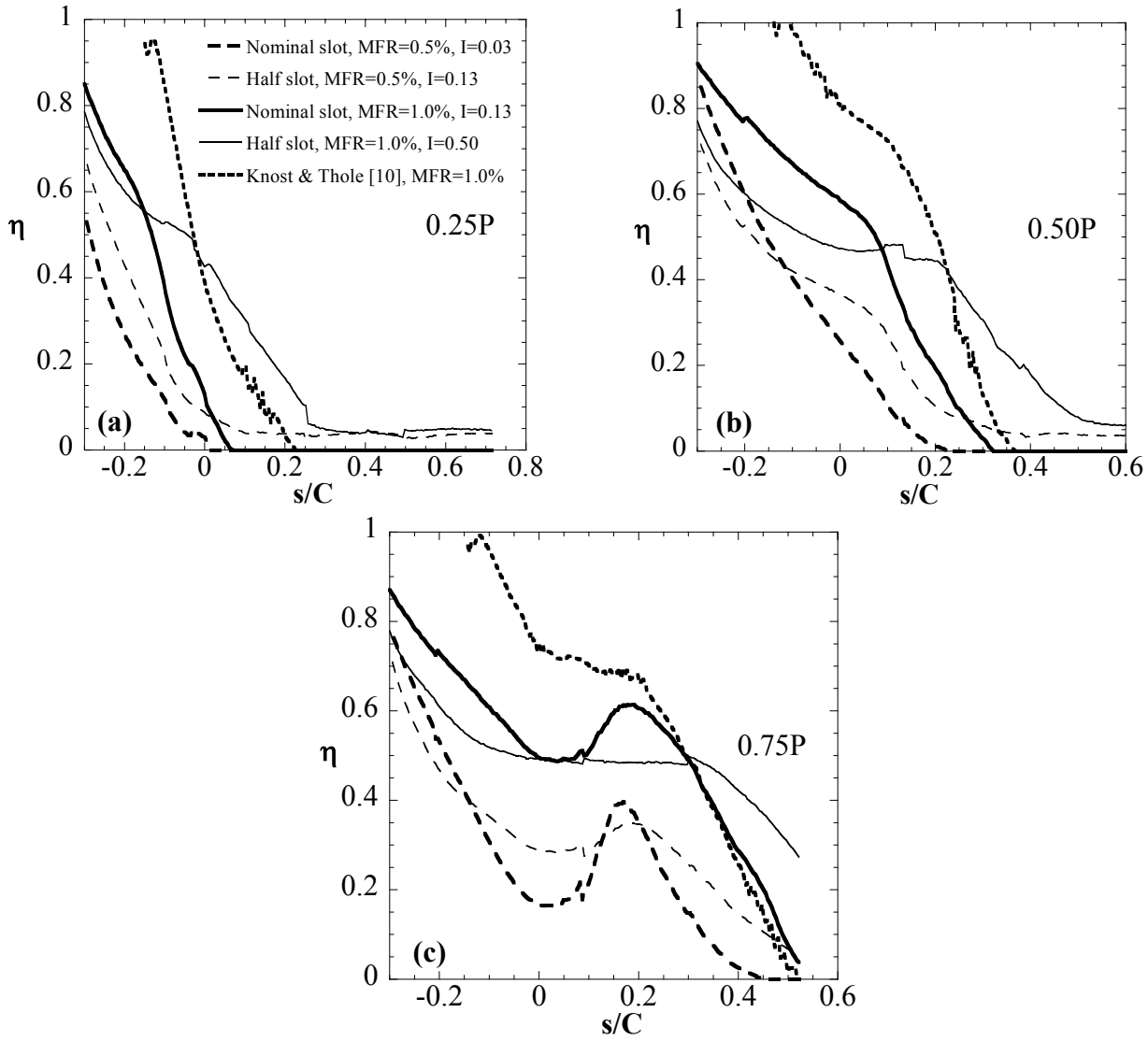


**Figure 1.7** **Adiabatic cooling effectiveness on the endwall from upstream slot flow, sampled along an inviscid streamline released from (a) 25% pitch, (b) 50% pitch, (c) 75% pitch.**

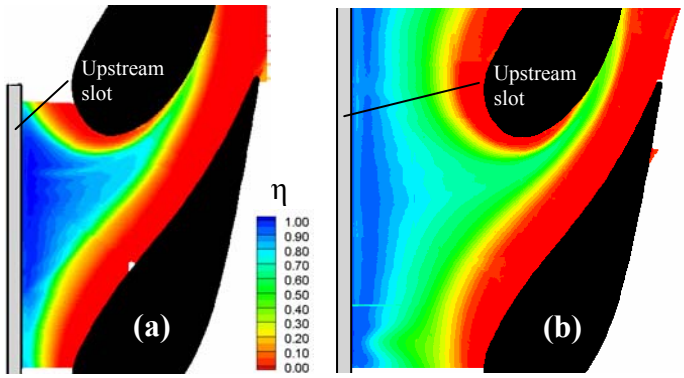


**Figure 1.8** **Contours of effectiveness for the nominal slot at 1.0% MFR for (a) Knost & Thole [10] (slot at $X/C_{ax}$=-0.38), and (b) this study (slot at $X/C_{ax}$=-0.77).**

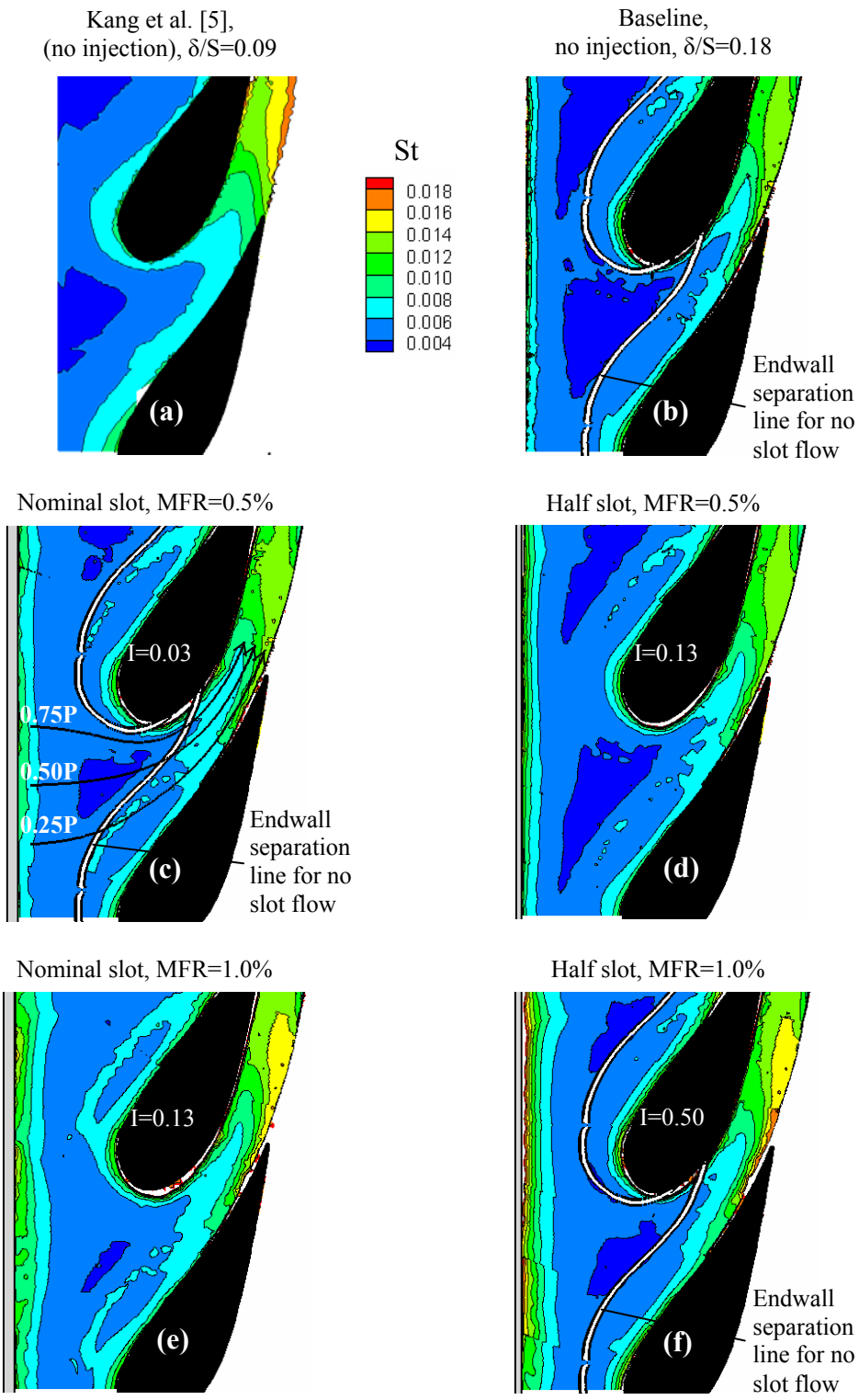


**Figure 1.9** **Contours of St for (a) Kang et al. [5] (no upstream slot); (b) baseline (no upstream slot); (c) nominal slot, MFR=0.5%; (d) half slot, MFR=0.5%; (e) nominal slot, MFR=1.0%; (f) half slot, MFR=1.0%.**

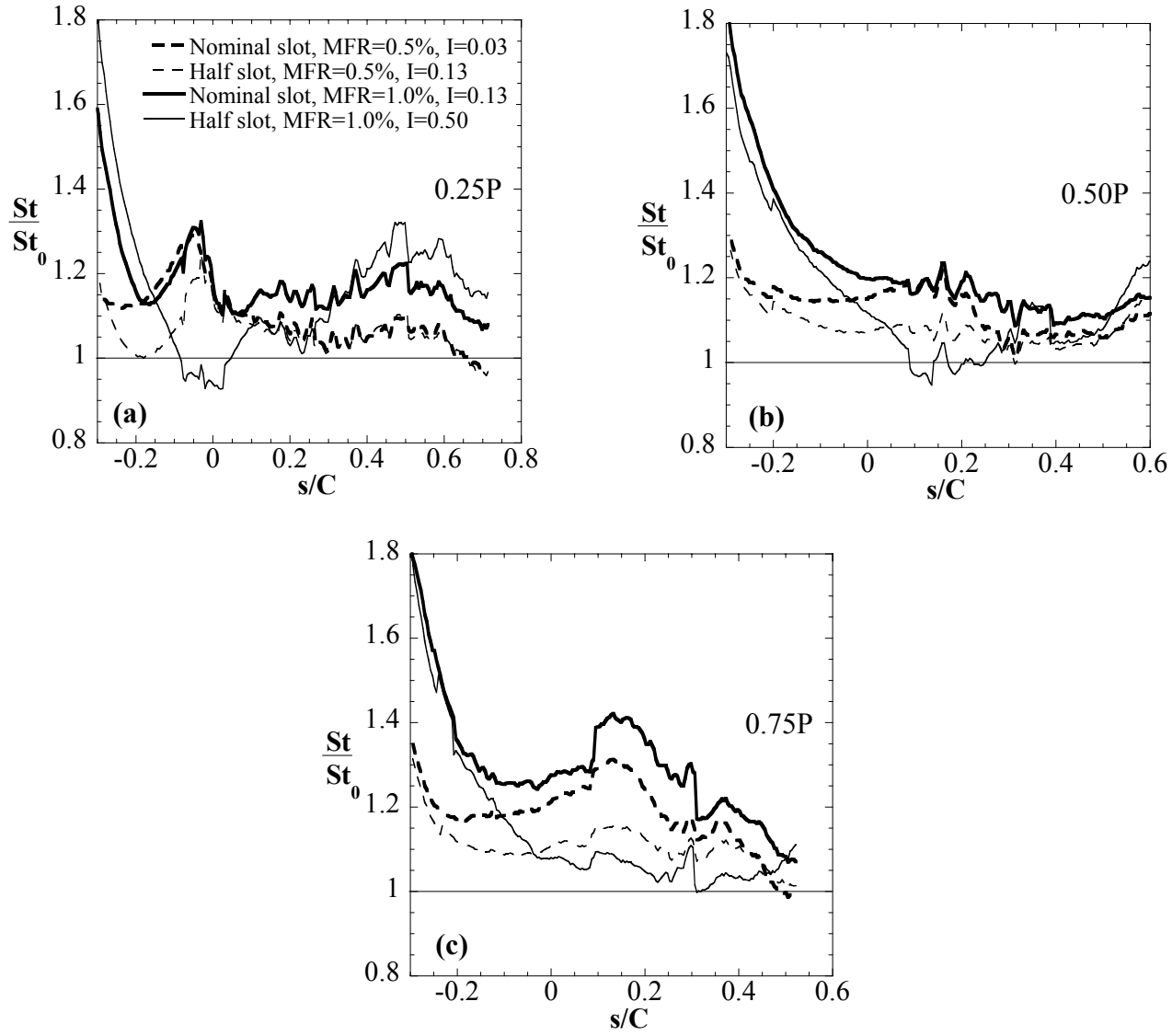


**Figure 1.10 Heat transfer augmentation on the endwall from upstream slot flow, sampled along an inviscid streamline released from (a) 25% pitch, (b) 50% pitch, (c) 75% pitch.**

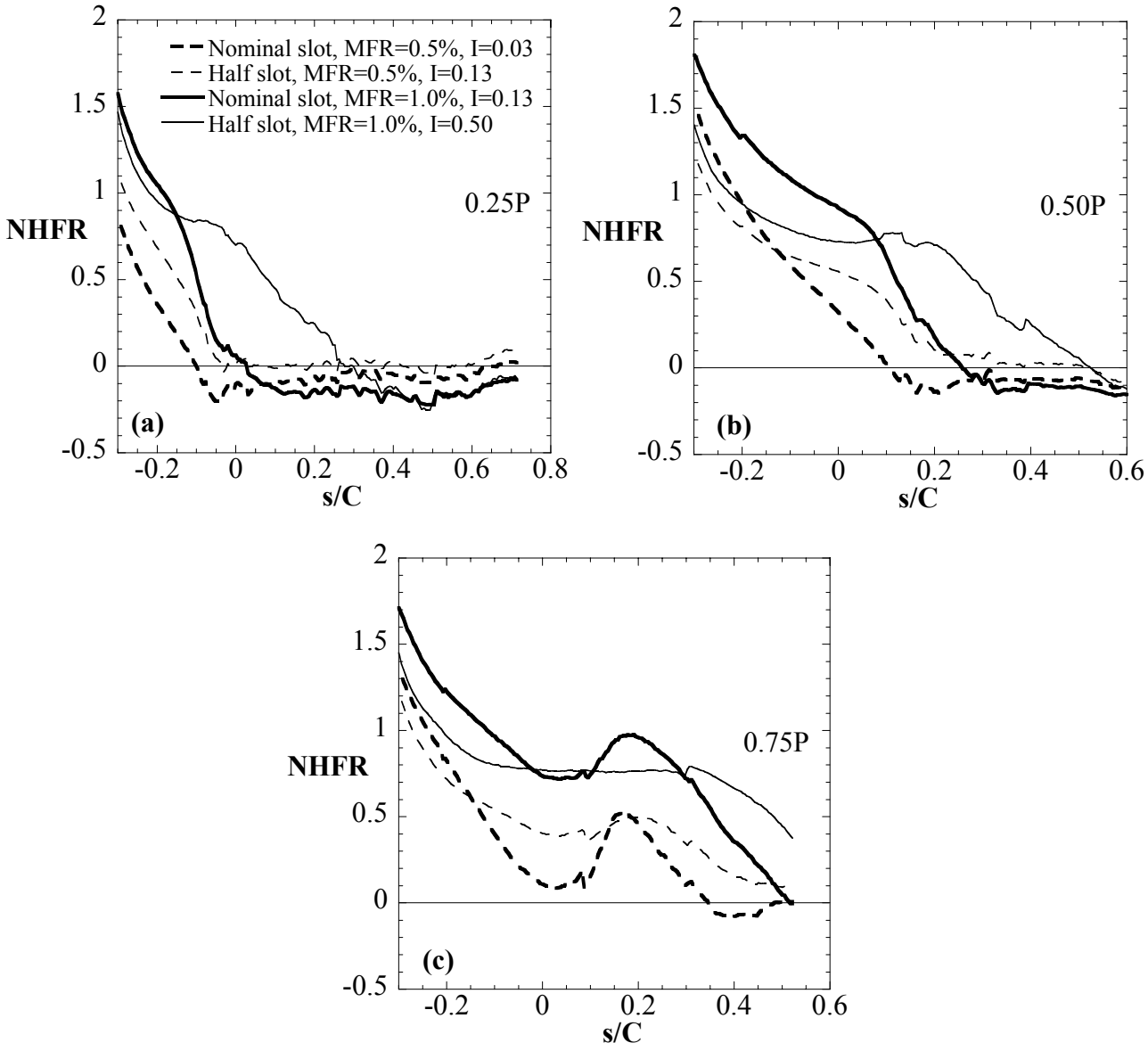


**Figure 1.11 Net heat flux reduction (NHFR) to the endwall from upstream slot flow, sampled along an inviscid streamline released from (a) 25% pitch, (b) 50% pitch, (c) 75% pitch.**

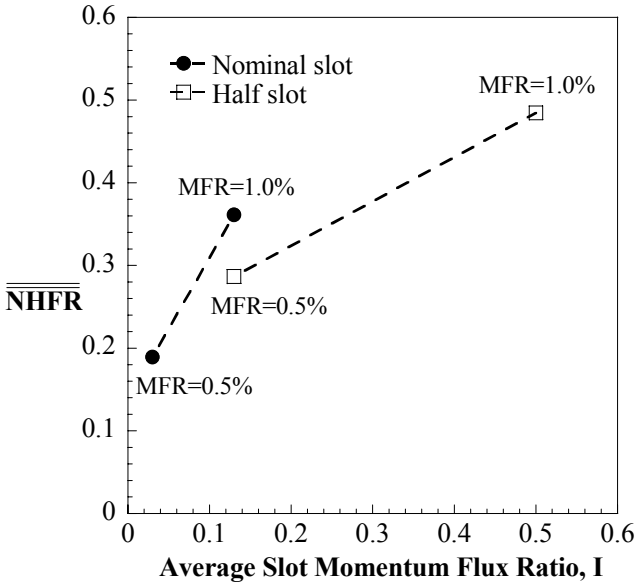


**Figure 1.12 Area-averaged net heat flux reduction (NHFR) to the endwall, as a function of upstream slot momentum flux ratio.**

## Paper 2:

# HEAT TRANSFER AND SHEAR STRESS FOR A NOZZLE GUIDE VANE ENDWALL WITH FILLETS AND COMBUSTOR-TURBINE GAP LEAKAGE FLOW

To be submitted to the ***2008 IGTI Conference****

### Abstract

Increasing the turbine inlet temperature to achieve high gas turbine efficiency and power output results in high heat loads on the nozzle guide vane in the turbine section. These heat loads are managed by cooling air bypassed from the compressor. The endwall poses particular cooling challenges because of the complex vortical secondary flow at the airfoil-endwall junction. Past studies have shown that a fillet at the airfoil-endwall junction can attenuate the development of secondary flow for aerodynamic and thermal benefit. Also, leakage flow from the gap between the combustor and turbine can provide cooling to the endwall; however, the combined effect of these two mechanisms has not been tested.

This study presents heat transfer, adiabatic cooling effectiveness, and shear stress on the endwall and fillet surfaces for a linear cascade with leakage flow from a flush slot placed upstream of the vanes. The addition of a fillet to the airfoil-endwall junction slightly reduced average heat transfer coefficients compared to an unfilleted endwall, with and without upstream slot leakage flow. A large fillet with a linear airfoil-to-endwall profile, however, displaced coolant around the vane, leading to poor coverage except for a high slot momentum flux ratio. Although shear stress magnitude without upstream slot flow was higher at the throat for the filleted endwall, the fillet reduced overturning at the throat associated with secondary flow.

*Co-author: Dr. Karen A. Thole, Mechanical and Nuclear Engineering Department, The Pennsylvania State University

## Introduction

Increases in gas turbine efficiency and power output can be achieved by increasing the temperature of the combustion products entering the nozzle guide vane in the turbine section. However, the high heat loads to the nickel superalloy material of the nozzle guide vane require significant cooling to maintain part strength and durability, given that the combustion gas temperature can be on the order of 300°C higher than the melting temperature. Air bled from the compressor section can be routed to the turbine for internal and external cooling.

The endwall region of a turbine vane or blade is particularly important to cool because of the presence of a complex flow that develops at the airfoil-endwall junction. Various flow models, including Langston [1], Sharma and Butler [2], Goldstein and Spores [3], and others, describe an approaching boundary layer that rolls up into a horseshoe vortex at the leading edge of the vane. The horseshoe vortex splits into suction and pressure side legs, and the pressure side leg develops into a larger passage vortex. These vortical structures, generally termed secondary flows, can be a large source of aerodynamic loss (30-50% according to Sharma and Butler [2]). Secondary flows also sweep coolant from the endwall and increase endwall heat transfer coefficients.

Several methods to control or eliminate secondary flows have been tested, including blowing, endwall contouring, and modifications of the leading-edge endwall-airfoil junction. Adding a fillet to the endwall-airfoil junction has been shown to be particularly successful in reducing total pressure loss and endwall heat transfer coefficients; see the following discussion of the results of Zess and Thole [4], Becz et al. [5], Lethander et al. [6], Han and Goldstein [7], and others.

In an engine, gaps are present between individually manufactured components, and cool air from the compressor is allowed to leak through the gaps. This prevents hot gas ingestion, and can provide some cooling to the part surface. A particular gap of interest for the work presented in this paper is between the combustor and the turbine. Leakage flow from this gap interacts with the secondary flow, and at high flow rates the coolant may promote secondary flow development. Furthermore, thermal expansion of the turbine over the large operational range of the engine can result in variations in the gap width that affect the leakage flow from the gap.

This paper presents experimental measurements of the combined effect of combustor-turbine interface leakage and a large leading-edge fillet on endwall heat transfer, adiabatic

cooling effectiveness, and shear stress. The objective of this study is to explore the interaction of the fillet with combustor-turbine gap leakage flow.

## Relevant Past Studies

Successful passive methods of controlling or eliminating horseshoe vortex development include three-dimensional endwall contouring and leading edge endwall-airfoil geometries. However, these methods are rarely considered simultaneously with film cooling, and in the case of an engine with a leakage interface, the interaction of leakage flow with endwall contouring or a fillet can result in unexpected behavior.

One of the more successful passive secondary flow control techniques has been modification of the endwall-airfoil junction. Sauer et al. [8] used an asymmetric leading edge bulb to intensify the suction side leg of the horseshoe vortex, which resulted in a 47% reduction in net aerodynamic losses. Zess and Thole [4] computationally studied several fillet designs, and experimentally tested a successful asymmetric linear-profile design. Measurements indicated elimination of the horseshoe vortex and an order of magnitude reduction in turbulent kinetic energy levels associated with vortex development. Becz et al. [5] investigated two bulbs based on the design of Sauer et al. [8], as well as an asymmetric elliptical fillet, and found that only the fillet reduced overall total mass-averaged pressure loss.

Other studies have focused on the thermal aspects of an endwall-airfoil juncture modification. Shih and Lin [9] performed computational studies on two fillet designs with and without swirl in the incoming flow profile. Their study indicated the largest reduction of heat transfer on the airfoil and endwall and the least overall aerodynamic penalty occurred with no fillet and inlet swirl. Lethander et al. [6] successfully integrated optimization software with a commercial CFD solver to design a relatively large fillet (with dimensions at the limits of their design space) that reduced adiabatic wall temperatures. Streamlines indicated elimination of the horseshoe vortex for the large fillet, although the fillet exhibited a slight increase in mass-averaged total pressure loss relative to an unfilleted endwall. Han and Goldstein [7] used naphthalene sublimation to infer heat transfer distributions on the endwall through the heat and mass transfer analogy. Their linear asymmetric fillet, based on the design of Zess and Thole [4], reduced the horseshoe vortex but resulted in increased heat transfer at the endwall-airfoil junction downstream of the fillet due to intensified corner vortices. The measurements of

Mahmood et al. [10] for four fillet geometries indicated that the fillets reduced the leading edge vortex size and lowered endwall heat transfer coefficients downstream of the fillets, with a concave circular geometry showing a slightly larger reduction in heat transfer than any of the other geometries. Total pressure losses, however, were not reduced with any of the fillets. In a related study, Saha et al. [11] presented computations for linear and circular profile fillets of the same geometry as Mahmood et al. [10]. Endwall Nusselt numbers were slightly reduced with the addition of a fillet, although there was no difference between the fillets. The fillets also resulted in reduced streamwise vorticity and turbulent kinetic energy, leading Saha et al. [11] to conjecture that a fillet weakened secondary flows.

Several significant studies have investigated the thermal and aerodynamic effect of leakage flow introduced through the combustor-turbine interface gap upstream of the nozzle guide vane. Blair's [12] measurements of endwall heat transfer and adiabatic cooling effectiveness from leakage flow through a two-dimensional flush slot upstream of the vane revealed that coolant accumulated at the suction side corner of the vane-endwall junction, and increased coolant flow rates resulted in better coverage. Endwall heat transfer coefficients, however, were not dramatically influenced by the leakage flow. A computational study by Knost and Thole [13] showed that near-wall streamlines became increasingly directed toward the pressure side of the vane as the flow rate through their two-dimensional flush slot was increased.

A two-part study by Burd and Simon [14] and Burd et al. [15] investigated the aerodynamic and thermal effect of leakage flow from a flush slot in a cascade with a streamwise-contoured endwall. The aerodynamic measurements of Burd and Simon [14] revealed that the slot exit velocity became more uniform across the vane pitch as the flow rate was increased, and that the addition of leakage flow did not impact the total pressure loss in the cascade. Burd et al. [15] concluded from their thermal measurements that coolant at low flow rates was strongly influenced by secondary flow, but coolant at a high flow rate of 3.2% provided optimum coverage because its high momentum enabled it to avoid being entrained by secondary flow vortices. Heat transfer coefficients measured at limited points in the passage did not change significantly with the addition of slot flow.

The series of studies by Kost and Nicklas [16], Nicklas [17], and Kost and Mullaert [18] presented aerodynamic and heat transfer measurements for upstream slot flow and discrete hole passage film cooling in a transonic cascade. Kost and Nicklas [16] and Nicklas [17] found that

leakage flow from their flush slot, positioned $0.2C_{ax}$ upstream of the vane, strengthened the horseshoe vortex and dramatically increased heat transfer coefficients. This was attributed to the slot injecting at the separation location on the endwall. In Kost and Mullaert's [18] subsequent study, the slot was positioned farther upstream (at $0.3C_{ax}$ upstream of the vane), which helped coolant stay close to the endwall and spread more uniformly.

Cardwell et al. [19] studied the effect of axial expansion of the combustor-turbine interface and found that adiabatic cooling effectiveness coverage area was a function of slot momentum flux ratio, but effectiveness levels were dependent on the slot mass flow ratio. Lynch and Thole [20] also concluded this for the same slot and airfoil geometry, even though their slot was located two times farther upstream of the vane. Moreover, the limit of the coolant coverage area correlated well with the endwall separation line. Lynch and Thole's [20] heat transfer coefficient results showed little variation with increasing slot flow.

This study is the first to present the combined effect of combustor-turbine interface leakage flow and a large fillet at the endwall-airfoil junction. Furthermore, no fillet studies to date have presented results for the fillet surface, which would be of interest to turbine designers since it is a surface that must be cooled.

## Experimental Facility and Methodology

Heat transfer, adiabatic cooling effectiveness, and shear stress were measured on the endwall of the nozzle guide vane test section in a closed-loop low-speed wind tunnel. The tunnel, illustrated in Figure 2.1 and previously described by Lynch and Thole [20], had an axial fan that drove the flow through the closed loop. A porous plate diverted some of the flow into bypass channels, where it could be further cooled to 20°C for film effectiveness studies. The core channel flow that was not diverted could be heated to 45°C with a 55kW heater bank, to simulate hot mainstream flow for the effectiveness measurements. For the friction coefficient and heat transfer coefficient studies, no flow heating or cooling was necessary.

A contraction section was located 2.9C upstream of the nozzle guide vane. The contraction reduced the flow area from 1.11 $m^2$ to 0.62 $m^2$ through symmetric 45° bounding walls. The nozzle guide vane test section is depicted in Figure 2.2. The test section contained two flow passages, defined by two full nozzle guide vanes and a third partial vane connected to a flexible wall. The flexible wall was adjusted to maintain the desired pressure distribution around

the center vane. The vanes, based on the midspan geometry of a commercial aircraft engine nozzle guide vane, were scaled by a factor of nine from the engine, and were manufactured from low-density polyurethane foam for low conductivity. The nozzle guide vane parameters are given in Table 2.1.

A turbulent boundary layer was measured at 0.63C upstream of the vane on the bottom endwall. The boundary layer had a thickness of $\delta/S=0.18$, a momentum thickness of $\theta/S=0.020$, a shape factor H=1.26, and a momentum Reynolds number $Re_\theta=4138$. The effect of high freestream turbulence was considered to be of secondary interest compared to the endwall leakage flow and leading edge geometries; thus, the tunnel nominal turbulence intensity and length scale for this study, measured at the cascade inlet, were 0.9% and 4 cm (0.07C), respectively.

*Combustor-Turbine Interface Geometry*

The leakage interface between a combustor and a turbine was modeled by a two-dimensional slot placed on the bottom endwall of the nozzle guide vane test section, as seen in Figure 2.2 and described in Lynch and Thole [20]. The interface will be referred to as an upstream slot in this paper. The leakage interface was based on the geometry of Cardwell et al. [19], who consulted industrial contacts to design a representative leakage interface. Note, however, that the upstream slot in this study, and that of Lynch and Thole [20], was located much farther upstream of the vane ($0.77C_{ax}$ in this study, compared to $0.38C_{ax}$ for Cardwell et al. [19]), to accommodate the large leading-edge endwall-airfoil geometries presented here. The slot extended across the entire pitch of the cascade.

To test the effects of engine axial thermal expansion on the leakage flow, two slot metering widths were tested. The nominal metering width, scaled to nine times that of the engine, was 1.43 cm (0.024C). The contracted slot width was 50% of the nominal metering width, and will be referred to as a half slot.

The leakage flow was supplied from a plenum located underneath the bottom endwall. The plenum supply was extracted from the top bypass channel of the wind tunnel by a blower (see Figure 2.1). To determine the average mass flow through the slot, the inviscid blowing ratio of the slot was multiplied by an assumed discharge coefficient of 0.6 (the commonly-accepted value for a sharp-edged orifice [21]). In this paper, mass flow through the slot is reported as a percentage of the mass flow entering a vane passage. Table 2.2 lists the coolant settings studied.

The coolant-to-mainstream density ratio was fixed at 1.1 for the adiabatic effectiveness measurements. Although the density ratio is lower than the typical value for an engine, the mass flow and slot width were based on industrial input, so the blowing and momentum flux ratios of the slot flow are expected to be representative of engine values. For the heat transfer coefficient measurements, the slot flow was maintained to within 0.1°C of the mainstream temperature.

*Endwall-Airfoil Fillet Designs*

Two large leading-edge fillet designs were chosen for comparison with a standard 90° endwall-airfoil junction. The two geometries, illustrated in Figure 2.3, were designed with a linear endwall-to-airfoil profile (referred to as a linear fillet), and an elliptical endwall-to-airfoil profile (referred to as an elliptical fillet). The geometry of the fillets followed the methodology of the computational optimization study by Lethander et al. [6]. The extent of the fillet outward from the vane, as well as the height of the fillet from the bottom endwall, was described by a half-cosine that was a function of the distance along the vane surface. The fillet design parameters included the maximum fillet extent and height (cosine amplitude), the locations of the maximum extent and height relative to the vane stagnation (cosine phase), and the maximum distance of the fillet around the vane (cosine half-period). This allowed the leading-edge fillets to merge smoothly into the nominal manufacturing fillet (1.1 cm radius [0.019C]) while still maintaining the vane gage point. For this study, the linear fillet and the elliptical fillet had the same design parameters, and only differed in their endwall-to-airfoil profile.

The linear and elliptical fillets were machined from the same low-density foam as the vane and instrumented with thermocouples. The fillets were positioned around the base of the vane airfoils and sealed using silicone. Note that the baseline unfilleted endwall did not have a manufacturing fillet at the base of the vane, since the small size of the manufacturing fillet did not have an impact on the endwall flowfield [6].

*Shear Stress Measurements*

Shear stress was measured on the endwall and linear fillet surface using the oil film interferometry (OFI) technique. OFI employs the shear rate of oil over a surface to quantitatively determine the wall shear, and was described in detail in Lynch and Thole [20]. Refer to Figure 2.4 for a depiction of the oil film development and a sample interferogram from the endwall measurements. The oil film is on the order of the wavelength of visible light, and its thickness is

measured using interferometry. The equation used in this study to calculate wall shear (in the form of a non-dimensional friction coefficient) is:

$$C_f = \frac{L_f \frac{\lambda}{2}\sqrt{n_{oil}^2 - n_{air}^2 \sin^2\theta_i}}{\int \frac{1}{2}\rho U_{\infty,in}^2 \frac{1}{\mu_{oil}} dt} \tag{2.1}$$

Eq. (2.1) is derived from a reduction of the Navier-Stokes equations for the oil film, applied along an endwall streamline (limiting streamline). The direction of the limiting streamline was determined in this study by the shear direction of the oil film at the measurement point (see Figure 2.4b). An order-of-magnitude analysis for the oil film using representative values pertinent to this study revealed that the shear stress was at least two orders of magnitude larger than the pressure gradient, gravity, or inertial terms. See Naughton and Sheplak [22] for a review of oil film interferometry and the implementation of OFI in cascades by Harrison [23] and Holley and Langston [24].

The average distance between interferogram bands ($L_f$) is determined from the period of a sine wave fitted to the pixel intensity profile along the limiting streamline direction, such as in the method of Holley and Langston [24]. The wavelength of light ($\lambda$) and the light incidence angle ($\theta_i$), which can be used to calculate the height of the oil film, are functions of the optical setup that produces the interferogram images. The oil viscosity ($\mu_{oil}$) and cascade inlet dynamic pressure are functions of the run time, since the oil viscosity is sensitive to temperature and the dynamic pressure varies from start-up to shut-down.

For implementation in the vane cascade, silicone oil droplets were applied to nickel foil patches adhered to the endwall and fillet surfaces. The nickel foil was 0.05mm thick and did not have an effect on the measurement of shear ($z^+<10$ for the highest shear measured). The dynamic pressure and flow temperature were recorded throughout the run. Note that a typical run length to obtain measurable interferograms was approximately twenty minutes, with start-up and shutdown transients being less than 45 seconds of that time. The tunnel air temperature generally varied less than 4°C during a run, but the oil viscosity temperature sensitivity was still accounted for by the correlation of Naughton and Sheplak [22].

The foil patches were carefully removed after a test and imaged in a fixture with a nearly monochromatic sodium vapor lamp ($\lambda$=589, 589.6 nm) to obtain the interferograms. Several tests were required to obtain over 1400 data points on the endwall, and 1400 data points on the linear

fillet surface. Unlike the linear fillet, the elliptical fillet has double curvature and its surface cannot be flattened without distortion (non-developable surface, see Figure 2.3b). Due to this problem, at this time no shear stress measurements have been obtained for the elliptical fillet.

Our implementation of the OFI method was benchmarked by measuring friction factors in fully developed flow in a square channel. Friction factor measurements agreed with textbook correlations to within 5% over a range of channel Reynolds numbers ($25{,}000 < ReDh < 45{,}000$).

The partial derivative method described by Moffat [25] was used to calculate uncertainties for the measurements of friction coefficient magnitude and direction. Magnitude uncertainty was estimated as $\partial C_f = \pm 5.8\%$ for both low ($C_f = 0.004$) and high ($C_f = 0.126$) values of friction coefficients, and was dominated by uncertainty in the interferogram spacing. Directional uncertainty was estimated as $\partial \Psi = \pm 2°$ for both high and low friction coefficient values.

*Heat Transfer Coefficient Measurements*

Measurements of heat transfer coefficients were taken on the endwall and fillet surfaces by imaging surface temperatures on constant heat flux plates via infrared thermography. Both the endwall and fillet heat flux plates contained 25 μm inconel elements embedded in a serpentine pattern between 75 μm of kapton, to which a 37 μm copper layer was attached. To eliminate the need for endwall cooling under the fillets, the endwall heater was designed with separate circuits under the fillets. These circuits were turned off when the fillets were installed. The endwall heaters were attached to a 2.54 cm thick sheet of closed-cell foam to reduce conduction losses. Heat flux plates were also attached to the linear fillet, since its surface is developable (can be reduced to two dimensions). Because of its double curvature (non-developable surface), the elliptical fillet surface cannot be flattened without distortion, which complicates the heat flux plate manufacturing process. At this time, heat transfer coefficient measurements have not been taken with the elliptical fillet.

In order to calibrate the thermography images, type-E thermocouples were embedded into the foam under the heat flux plates and connected thermally to the heaters by thermal cement. A conduction bias of approximately 0.7°C between a bottom-mounted thermocouple and the top-surface IR measurement, due to heater thermal resistance, was accounted for by a one-dimensional correction. For all heaters, the top copper surface was painted flat black for high emissivity. Markers were etched into the paint near the thermocouples in order to locate the thermocouples and perform image transformation.

Spatially-resolved surface temperatures on the bottom endwall were obtained with an infrared camera mounted on the top endwall. An uncertainty analysis revealed that five images should be taken and averaged at each of the twenty locations around the cascade, where each image is also an average of 16 frames captured by the camera. The spatial integration of the camera was approximately 0.17 mm (0.0012C), and the camera frame size was 240x320 pixels. Image post-calibration for surface emissivity and reflected temperature was performed by matching the temperature at the thermocouple locations in the image to the output of the thermocouples. Calibrated images and thermocouples generally agreed to within 0.86°C.

The three-dimensionality of the fillet surface required a perspective distortion correction technique, since the portions of the fillet closer to the camera appear larger in the IR camera image. A correction was performed by placing a grid on the fillet surface and imaging it with the IR camera. An in-house program mapped the two-dimensional image pixels to the known coordinates of the gridpoints to remove the distortion. The camera location at a top endwall image port was fixed for all tests, so that the pixel mapping routine at each port could be used for subsequent data collection. The variability due to slight misalignment of the camera was less than three pixels (0.004C).

Heat flux to the endwall and fillets was determined by measuring the power supplied to the heater circuits and dividing by the circuit areas. The current through each circuit was determined by measuring voltage across a precision resistor (1Ω) in series with the circuit. Radiation and conduction corrections were performed locally, with the highest corrections occurring at the highest surface temperatures. The maximum corrections were 0.2% and 21% of the input power for conduction and radiation, respectively.

Overall uncertainty in Stanton number was estimated as $\partial St=\pm 0.00011$ (3.3%) at a St value of 0.003, and $\partial St=\pm 0.0009$ (7.5%) at a St value of 0.011, with the largest contribution from the surface temperature measurements ($\partial T=\pm 0.91$°C).

*Adiabatic Effectiveness Measurements*

Adiabatic wall temperatures due to upstream slot coolant were measured on the bottom endwall of the cascade with the IR camera. The bottom endwall was manufactured from 2.54 cm thick closed-cell foam to reduce conduction errors. Type-E thermocouples were embedded in the foam surface for calibration of the thermography measurements. The endwall and fillets

were painted using flat black paint for high emissivity. Infrared-reflective finishing nails were used as transformation markers in the thermography images.

Image capture and post-calibration was performed in the same way as for the heat transfer coefficient measurements. The thermocouples and the calibrated images generally agreed to within 0.3°C. The perspective distortion correction for the three-dimensionality of the fillet surfaces was also applied to these measurements.

A one-dimensional correction for endwall conduction effects was applied to all adiabatic effectiveness measurements. The resulting η correction was 0.14 at η=0.75 measured downstream of the slot, and 0.05 for η=0.07 measured at the exit of the vane passage.

Uncertainty in the measurements of adiabatic cooling effectiveness was estimated by the partial derivative method. Overall uncertainty in adiabatic effectiveness was estimated to be $\partial\eta=\pm0.036$ at a η value of 0.1, and $\partial\eta=\pm0.026$ at a η value of 0.8. The largest contribution to overall uncertainty was the measurement of adiabatic surface temperatures with the IR camera ($\partial T_{aw}=\pm0.51$°C). The adiabatic surface temperature uncertainty was lower than the heat flux plate surface temperature uncertainty because of a higher bias error in the method of heat flux plate temperature measurements.

## Discussion of Results

The measurements of shear stress magnitude and direction without upstream slot flow, for the unfilleted endwall and the endwall with a linear fillet, will be discussed first. A review of the heat transfer coefficient measurement results for an endwall with and without a linear fillet and upstream slot flow will follow. Finally, experimental measurements of adiabatic cooling effectiveness from an upstream slot in the presence of no fillet, a linear fillet, and an elliptical fillet are discussed.

### *Wall Shear Stress without an Upstream Slot*

The oil film interferometry method described earlier provided measurements of endwall and fillet surface shear stress, which were non-dimensionalized as friction coefficients. As described earlier, the difficulty in placing foil patches on the non-developable surface of the elliptical fillet precluded shear stress measurements for that geometry. Figure 2.5 presents contours of friction coefficient magnitude. The contours for the endwall with the linear fillet (Figure 2.5b) show surprising similarities to the contours from an endwall without a fillet (Figure

2.5a), in the leading edge region. The linear fillet, however, produces higher friction coefficient magnitudes in the throat region as compared to the unfilleted endwall. This is not unexpected since the linear fillet reduces the flow area in regions of the passage and thus accelerates the flow more rapidly than a passage without a fillet.

The presence of the fillet influences the path of the secondary flow, as seen by examining the endwall streamlines in Figure 2.6. The endwall streamlines were calculated from the measured shear stress vectors. The saddle point at the leading edge in the unfilleted endwall measurements (red streamlines in Figure 2.6) is the location of the horseshoe vortex roll-up, where incoming flow separates from the endwall and splits around the vane. This feature appears to be shifted upstream when the linear fillet is present (see black streamlines). Furthermore, at the leading edge of the fillet near the endwall-fillet junction, the streamlines are directed down the fillet surface toward the endwall-fillet junction, possibly due to the roll-up of a small vortex at this location. Further in the passage, streamlines are generally directed around the base of the fillet.

In the throat region, the endwall streamlines for the unfilleted endwall sweep from the pressure side to the adjacent vane suction side. This feature is a consequence of the cross-passage pressure gradient. For the linear fillet, the endwall streamlines are slightly less directed toward the suction side of the adjacent vane, as compared to the unfilleted endwall. Figure 2.7 presents the yaw angle of the endwall streamline direction across the throat, compared to the inviscid streamline yaw angle from the midspan flowfield of a FLUENT 6.2 [26] simulation of the unfilleted vane cascade. The error bars shown for the measurements in Figure 2.7 correspond to the estimated 2° uncertainty in shear stress vector direction. Note from Figure 2.7 that the passage vortex causes flow near the wall to be turned more than in the inviscid freestream. The linear fillet, however, reduces the overturning of the flow near the endwall, compared to the unfilleted endwall. This may be due to a reduction in passage vortex strength, or at least a disruption in the passage vortex flow. Lethander et al. [6] presented the computed secondary flow field at a plane near the throat (plane SS2, see Figure 2.8), which showed that their large linear fillet (of the same design as in this study) eliminated the passage vortex.

*Heat Transfer Coefficients without an Upstream Slot*

Heat transfer coefficients were measured for the endwall with and without a linear fillet installed, to determine the effect of the fillet on the endwall heat transfer. Recall that heat transfer

measurements were not taken for the elliptical fillet. Figure 2.9 presents contours of Stanton number on the endwall and fillet surfaces. Although there do not appear to be dramatic changes in the overall level of heat transfer to the endwall with the addition of a fillet, the heat transfer distribution is different. The region of low heat transfer at the passage entrance is shifted toward the center of the passage in the case of the linear fillet. Also, low heat transfer is seen on the pressure side surface of the linear fillet.

Quantitative comparisons of endwall results were obtained by extracting endwall values along the paths of inviscid streamlines obtained from a CFD prediction of the vane flowfield with FLUENT 6.2 [26]. Streamlines were released 0.3C upstream of the cascade at mid-span of the vane from three pitch locations, corresponding to Y/P = 0.25, 0.50 and 0.75 as shown in Figure 2.9a. These streamlines are denoted as 0.25P, 0.50P, and 0.75P, respectively. The leading edge stagnation streamline path was also obtained, and is denoted as STAG. Extracted endwall results (see Figure 2.10) are presented as a function of distance along each streamline, non-dimensionalized so that s/C=0 corresponds to where the streamline would cross a pitchwise line connecting adjacent vane stagnation points.

The leading edge stagnation region in the unfilleted case (Figure 2.9a) demonstrates the well-documented increase in Stanton number approaching the vane stagnation, associated with the roll-up of the horseshoe vortex. For the linear fillet, a slight increase in heat transfer is seen at the fillet-endwall junction. This is likely due to the small vortex indicated by the endwall streamline results presented earlier. The maximum surface Stanton number as the flow approaches the vane, however, is not as high as the maximum Stanton number for the unfilleted endwall. In Figure 2.10, this trend is shown quantitatively by comparing Stanton numbers extracted along the path of the inviscid streamline approaching the vane stagnation (STAG, refer to Figure 2.9a). Although the linear fillet exhibits a peak in Stanton number at the endwall-fillet junction, the fillet leads to lower heat transfer very near the vane, suggesting that the horseshoe vortex scouring action has been attenuated by the fillet.

As was seen in the shear stress measurements, the acceleration of the flow in the cascade due to the fillet blockage is manifested in Figure 2.9 as increased Stanton numbers (based on inlet mainstream velocity) at the throat region, compared to an unfilleted endwall. Figure 2.11 shows heat transfer coefficient values extracted across the throat for the unfilleted and filleted endwall. Note that the fillet leads to more uniform Stanton numbers across the throat as

compared to the unfilleted endwall, which is important for reducing local hot spots on the endwall.

*Heat Transfer Coefficients with Upstream Slot Flow*

Heat transfer coefficients were also measured for various upstream slot blowing rates and slot widths, and are presented in Figure 2.12. Comparison of Figure 2.12 with Figure 2.9 for no upstream slot flow reveals that the leakage flow at any flow rate slightly increases heat transfer coefficients relative to the no blowing cases, for both the unfilleted and filleted endwall. For a given slot width and mass flow ratio in Figure 2.12, however, the linear fillet appears to slightly reduce endwall heat transfer compared to an unfilleted endwall, in agreement with the conclusions from the heat transfer measurements without upstream slot blowing presented earlier.

The effect of increased mass flow from the nominal slot is shown in Figures 2.12a and 2.12c for the unfilleted endwall, and Figures 2.12e and 2.12g for the endwall with the linear fillet. Heat transfer coefficients show a slight increase throughout the passage, with the most obvious increases at the entrance of the cascade between the vanes, at the leading edge of the linear fillet, and in the wake of the vane when the slot mass flow increases from 0.5% to 1.0%. Figure 2.13 is a plot of heat transfer coefficient augmentation from upstream slot blowing, where $St_0$ is the heat transfer without blowing for the same endwall-airfoil geometry, along the 0.50P streamline through the passage. Note that in the shifted streamline coordinate system used for the endwall data extraction, the centerline of the upstream slot is located at s/C=-0.36. Endwall data is not extracted directly downstream of the slot, but rather starting at s/C=-0.3, in order to avoid the high measurement uncertainty at the start of the thermal boundary layer in the heat transfer coefficient measurements. The heat transfer augmentation due to slot leakage flow plotted in Figure 2.13 indicates that increasing the slot mass flow rate results in higher heat transfer augmentation. For a given slot flow rate, the unfilleted endwall experiences higher heat transfer augmentation than the endwall with the linear fillet; thus, the fillet helps to slightly reduce the detrimental effect of the slot flow on endwall heat transfer coefficients.

In an engine, a thermal expansion incident that reduces the upstream slot metering width would reduce mass flow through the slot, since the pressure ratio across the leakage interface is typically maintained. This effect is shown by comparing Figures 2.12b and 2.12c for the unfilleted endwall, and Figures 2.12f and 2.12g for the linear fillet. Contraction of the slot width

by 50% results in a reduction in slot mass flow from 1.0% to 0.5%, but also results in a slight reduction in heat transfer coefficient levels in the passage. Figure 2.14 also shows this trend along the 0.50P streamline path through the passage. For both the filleted and unfilleted endwalls, contraction of the slot width (and the subsequent reduction in slot mass flow) reduces the heat transfer augmentation in the passage. The acceleration of the slot leakage flow when the slot metering width is contracted may cause less turbulent interaction with the near-wall external flow and subsequently lower heat transfer levels.

The effect of slot contraction while maintaining the slot mass flow ratio requires a higher momentum flux through the contracted slot. This case is perhaps of more academic than practical interest in modern turbine engine cooling situations, but does provide some additional insight into the flow physics. From the contours of Figure 2.12, it is apparent for the linear fillet that contracting the slot width while maintaining 0.5% leakage flow through the slot (Figures 2.12e and 2.12f) does not have a large effect on heat transfer coefficient levels. In contrast, contracting the slot width while maintaining 1.0% slot mass flow (Figures 2.12g and 2.12h) results in a noticeable change in contour levels, particularly near the leading edge of the fillet. This trend is also shown in Figure 2.15, where the augmentation for the endwall with the linear fillet is plotted along the inviscid stagnation streamline (STAG) described earlier. Contraction of the slot width while maintaining a low slot mass flow of 0.5% does not result in a difference in augmentation, whereas contraction of the slot while maintaining 1.0% slot mass flow results in a dramatic decrease in augmentation due to the contracted slot flow. In the case of low slot mass flow from the nominal or contracted slots, the momentum of the coolant may not be large enough to interfere with the near-wall flowfield imposed by the fillet, and thus the convective heat transfer augmentation would not be expected to be largely different. In contrast, the high mass flow rate from the contracted slot requires a large momentum flux ratio and the slot flow may act more like a jet.

Area-weighted averages of the surface heat transfer coefficient results are shown in Figure 2.16. Note that a comparison of area-averaged results for the unfilleted and filleted endwall is complicated by the three-dimensionality of the linear fillet. In this study, the unfilleted endwall area being considered was one passage, starting at $X/C_{ax}$=-0.61 (same starting location as the streamlines in Figure 2.9) and ending at $X/C_{ax}$=1.06. The endwall area-average for the filleted vane used the same axial extents as for the unfilleted endwall, but the heat transfer

coefficients on the fillet were weighted by the surface area of the fillet. This resulted in an increase of 8.2% in total surface area being considered for the filleted endwall, as compared to the unfilleted endwall. Note, however, that the linear fillet actually reduces the total surface area of the vane-endwall junction (the length of the hypotenuse of a triangle is less than the sum of the lengths of each of its sides) and thus a fillet reduces the overall area that must be cooled. The tests performed in this study did not consider the vane surface, since the focus was on the endwall measurements.

Despite a larger total area being considered, for a given upstream leakage flow configuration in Figure 2.16, the addition of the linear fillet to the endwall-airfoil junction produces a reduction in average surface heat transfer coefficients of more than 11%. Also, the effect of adding upstream leakage flow to the unfilleted endwall, or to the endwall with the linear fillet, increases the average surface heat transfer. Increasing the slot mass flow rate increases the average heat transfer, while contraction of the slot width at a given mass flow rate slightly reduces the average heat transfer.

*Adiabatic Effectiveness Levels from an Upstream Slot*

Adiabatic cooling effectiveness measurements were obtained for upstream slot leakage flow with no fillet, a linear fillet, and an elliptical fillet at the endwall-airfoil junction, and are presented in Figure 2.17. The primary feature common to all of the measurements is a region of low effectiveness around the vane, into which the upstream leakage coolant does not penetrate. This region is a result of the roll-up of the horseshoe vortex, which acts as a barrier to the upstream coolant. Thus, modern turbine designs typically require discrete-hole film cooling in the hot region. Lynch and Thole [20] showed that for low upstream slot leakage flow rates, the limit of the upstream coolant penetration toward the base of the vane correlated well with the separation line on the endwall obtained from friction coefficient measurements without upstream slot flow.

The addition of a linear fillet to the endwall, at a given slot width and a low mass flow rate of 0.5%, appears to displace the upstream slot coolant from the leading edge and pressure side of the vane and force it between the fillets, as seen by comparing Figures 2.17a and 2.17e, or Figures 2.17b and 2.17f. Unfortunately, this is not a desirable coolant coverage pattern since it produces high lateral gradients in wall temperature on the endwall, and little to no cooling on the fillet surfaces. The elliptical fillet shows less dramatic displacement of coolant around the vane

than the linear fillet, but the coolant coverage is still not quite as extensive as for the unfilleted endwall. Figure 2.18 presents effectiveness values extracted along the STAG streamline path for the 0.5% slot mass flow cases. Along this streamline, for either the nominal or half slot widths at 0.5% mass flow, the linear fillet produces the lowest values of effectiveness, with the elliptical fillet showing slightly higher effectiveness than the linear fillet, but lower effectiveness than for an unfilleted endwall. However, along the 0.50P streamline path in Figure 2.19, the linear fillet leads to higher effectiveness levels than the unfilleted endwall downstream of s/C=0.05, because of how the linear fillets force the low-momentum coolant to travel between them.

Although the coolant displacement due to the linear fillet blockage is also apparent for leakage flow from the nominal slot at 1.0% MFR (Figure 2.17g), the effect of slot width contraction at this mass flow ratio (Figure 2.17h) results in coolant with high momentum that can penetrate close to the vane. This effect of slot coolant penetration at a high momentum flux ratio (I=0.50) was also noted in Lynch and Thole [20] for the unfilleted endwall (Figure 2.17d).

In general, the elliptical fillet shows similar coolant coverage as for the unfilleted endwall (see Figures 2.17a and 2.17i, or 2.17d and 2.17l), with slightly lower local effectiveness levels (compare effectiveness levels along the STAG streamline path in Figure 2.18). The smoothly curved shape of the elliptical fillet results in less flow blockage than the linear fillet, and thus it does not strongly dictate the endwall-airfoil junction flow pattern.

As was described in Lynch and Thole [20] for an unfilleted endwall, the effect of upstream slot contraction due to engine thermal expansion leads to lower local effectiveness levels, but similar extent of coolant coverage. This trend also holds for an endwall with a linear or elliptical fillet (compare Figures 2.17f and 2.17g for the linear fillet, or Figures 2.17j and 2.17k for the elliptical fillet). Figure 2.19 shows that the higher mass flow (1.0% MFR) from the nominal slot, at a momentum flux ratio of I=0.13, provides more cooling to the endwall than for the half slot (0.5% MFR).

Area-weighted averages of the effectiveness data were performed the same way as for the heat transfer coefficient data. Figure 2.20 presents the average cooling effectiveness for each of the upstream slot coolant situations tested. Several trends are noted from this figure. For a given mass flow rate, as the slot contracts, the average cooling effectiveness increases. Also, for matched momentum flux, the contracted slot has lower average effectiveness than the nominal slot since the contracted slot ejects less coolant (0.5% MFR, compared to 1.0% MFR from the

nominal slot). Adding a linear fillet to the vane-endwall junction tends to lower average cooling effectiveness dramatically compared to the unfilleted endwall; at 0.5% MFR from the nominal slot, the linear fillet causes a 43% reduction in average effectiveness compared to the unfilleted endwall. The elliptical fillet performs better than the linear fillet in terms of average effectiveness, but still has lower average effectiveness than an unfilleted endwall. Finally, at the highest slot momentum flux ratio tested (I=0.50), the linear and elliptical fillets cause nearly the same average effectiveness, but that level is 22% lower than the average effectiveness for an unfilleted endwall.

## Conclusions

Measurements of shear stress and heat transfer were obtained for an endwall with and without a large linear-profile fillet at the endwall-airfoil junction. Heat transfer and adiabatic cooling effectiveness due to leakage flow from a flush slot placed upstream of the cascade were also obtained for an endwall with no fillet, the large linear-profile fillet, and a similar large elliptical-profile fillet.

For a linear-profile fillet and no slot leakage, flow acceleration due to the blockage of the large linear fillet increased shear stress in the throat of the cascade as compared to an unfilleted endwall. However, the yaw angles of the endwall streamlines were reduced with the linear fillet, which may indicate a reduction in the strength of the passage vortex. Heat transfer was also higher at the throat for an endwall with a linear fillet compared to an unfilleted endwall, but other regions of the endwall showed lower heat transfer levels with a linear fillet. Moreover, the average heat transfer was less for the endwall with a linear fillet.

Addition of leakage flow to the endwall from an upstream slot increased local heat transfer relative to the no blowing case, and increasing the slot flow rate further increased heat transfer. The half slot flow, at the same momentum flux as the nominal slot flow, resulted in lower local heat transfer levels. For a given slot flow rate or metering width, the presence of the linear fillet always resulted in a reduction in the average surface heat transfer coefficient, suggesting that the benefit of the fillet was still evident in the more realistic interface leakage flow situation studied here.

Unfortunately, neither the linear fillet nor the elliptical fillet performed well in terms of the adiabatic cooling effectiveness levels of leakage flow from the flush slot configuration. The

linear fillet tended to displace slot coolant and channel it between the fillets, which resulted in high effectiveness gradients. The elliptical fillet did not change the coverage of the coolant as much as the linear fillet, but still tended to displace coolant away from the vane as compared to an unfilleted endwall. Note that the leakage coolant behavior may also be a function of the upstream slot location relative to the vane; coolant at the highest momentum flux ratio tested (I=0.50) had sufficient momentum to be able to penetrate close to the vane and provide significant coverage.

These results indicate that the use of a large fillet at the endwall-airfoil junction contributes to reduced endwall heat transfer, but low-momentum leakage flow from the combustor-turbine interface gap may be negatively impacted by the blockage of the fillet. Thus, engine designers must carefully consider how a method of secondary flow control integrates with the complex flowfield resulting from gap interface leakage.

## Acknowledgments

The authors would like to thank the National Science Foundation's GOALI program for funding this research (Grant No. 0412971). We would also like to acknowledge our partners in the GOALI program: Joel Wagner and Peter Tay (Pratt & Whitney), and Dr. Lee Langston and Brian Holley (University of Connecticut).

## Nomenclature

| | |
|---|---|
| C | true chord of stator vane |
| $C_{ax}$ | axial chord of stator vane |
| $C_f$ | friction coefficient, $C_f = \tau_w \Big/ \frac{1}{2}\rho U^2_{\infty,in}$ , see Eq. (2.1) |
| $C_p$ | heat capacity at constant pressure |
| h | heat transfer coefficient |
| $h_{oil}$ | height of oil film |
| I | average momentum flux ratio, $I = \rho_c U_c^2 \Big/ \rho_\infty U^2_{\infty,in}$ |
| $L_f$ | spacing between oil film interferogram bands (fringes) |
| M | average blowing ratio, $M = \rho_c U_c / \rho_\infty U_{\infty,in}$ |
| MFR | mass flow ratio, $MFR = \dot{m}_c / \dot{m}_{in}$ |
| n | index of refraction |
| P | pitch of stator vane, or pressure |
| $Re_{Dh}$ | Reynolds number based on hydraulic diameter |

| | |
|---|---|
| $Re_{in}$ | inlet Reynolds number, $Re_{in} = CU_{\infty,in}/\nu$ |
| $Re_\theta$ | momentum thickness Reynolds number, defined as $Re_\theta = \theta U_{\infty,in}/\nu$ |
| s | distance along a streamline |
| S | span of stator vane |
| St | Stanton number, $St = h/\rho C_p U_{\infty,in}$ |
| t | time |
| T | temperature |
| U | axial velocity |
| X, Y, Z | vane coordinates, where X is turbine axial direction |

*Greek*

| | |
|---|---|
| $\delta$ | boundary layer thickness |
| $\eta$ | adiabatic cooling effectiveness, $\eta = (T_\infty - T_{aw})/(T_\infty - T_c)$ |
| $\theta$ | momentum thickness |
| $\theta_i$ | incident light angle |
| $\lambda$ | light wavelength of sodium vapor lamp |
| $\mu_{oil}$ | dynamic viscosity of oil |
| $\nu$ | kinematic viscosity |
| $\rho$ | density |
| $\tau_w$ | wall shear stress |
| $\varphi$ | phase difference of light rays, $\varphi = (T_\infty - T_c)/(T_\infty - T_w)$ |
| $\Psi$ | yaw angle (X-Y plane) relative to streamwise direction |

*Subscripts/Superscripts*

| | |
|---|---|
| 0 | baseline conditions (no blowing) |
| aw | adiabatic wall |
| c | coolant conditions |
| in | inlet conditions |
| s | streamline coordinate |
| $\infty$ | local freestream conditions |
| + | scaling based on inner variables |

## References


[1] Langston, L.S., 1980, "Crossflows in a Turbine Passage," *J of Engineering for Power*, Vol. 102, pp. 866-874.

[2] Sharma, O.P. and Butler, T.L., 1987, "Predictions of Endwall Losses and Secondary Flows in Axial Flow Turbine Cascades," *J of Turbomachinery*, Vol. 109, pp. 229-236.

[3] Goldstein, R.J. and Spores, R.A., 1988, "Turbulent Transport on the Endwall in the

Region Between Adjacent Turbine Blades," *J of Heat Transfer*, Vol. 110, pp. 862-869.

[4] Zess, G.A., and Thole, K.A., 2002, "Computational Design and Experimental Evaluation of Using a Leading Edge Fillet on a Gas Turbine Vane," *J of Turbomachinery*, Vol. 124, pp. 167-175.

[5] Becz, S., Majewski, M.S., and Langston, L.S., 2004, "An Experimental Investigation of Contoured Leading Edges for Secondary Flow Loss Reduction," ASME Paper GT2004-53964.

[6] Lethander, A.T., Thole, K.A., Zess, G.A., and Wagner, J., 2003, "Optimizing the Vane-Endwall Junction to Reduce Adiabatic Wall Temperatures in a Turbine Vane Passage," ASME Paper GT2003-38940.

[7] Han, S., and Goldstein, R.J., 2006, "Influence of Blade Leading Edge Geometry on Turbine Endwall Heat (Mass) Transfer," *J of Turbomachinery*, Vol. 128, pp. 798-813.

[8] Sauer, H., Müller, R., and Vogeler, K., 2001, "Reduction of Secondary Flow Losses in Turbine Cascades by Leading Edge Modifications at the Endwall," *J of Turbomachinery*, Vol. 123, pp. 207-213.

[9] Shih, T. I-P., and Lin, Y-L., 2001, "Controlling Secondary-Flow Structure by Leading-Edge Airfoil Fillet and Inlet Swirl to Reduce Aerodynamic Loss and Surface Heat Transfer," *J of Turbomachinery*, Vol. 125, pp. 48-56.

[10] Mahmood, G.I., Gustafson, R., and Acharya, S., 2005, "Experimental Investigation of Flow Structure and Nusselt Number in a Low-Speed Linear Blade Passage With and Without Leading-Edge Fillets," *J of Heat Transfer*, Vol. 127, pp. 499-512.

[11] Saha, A., Mahmood, G.I., and Acharya, S., 2006, "The Role of Leading-Edge Contouring on End-Wall Flow and Heat Transfer: Computations and Experiments," ASME Paper

GT2006-91318.

[12] Blair, M.F., 1974, "An Experimental Study of Heat Transfer and Film Cooling on Large-Scale Turbine Endwalls," *J of Heat Transfer*, pp. 524-529.

[13] Knost, D. G., and Thole, K. A., 2005, "Adiabatic Effectiveness Measurements of Endwall Film-Cooling for a First Stage Vane," *J of Turbomachinery*, Vol. 127, pp. 297-305.

[14] Burd, S.W., and Simon, T.W., 2000, "Effects of Slot Bleed Injection Over a Contoured Endwall On Nozzle Guide Vane Cooling Performance: Part I – Flow Field Measurements," 2000-GT-199.

[15] Burd, S.W., Satterness, C.J., and Simon, T.W., 2000, "Effects of Slot Bleed Injection Over a Contoured Endwall On Nozzle Guide Vane Cooling Performance: Part II - Thermal Measurements," 2000-GT-200.

[16] Kost, F. and Nicklas, M., 2001, "Film-Cooled Turbine Endwall in a Transonic Flow Field: Part I-Aerodynamic Measurements," *J of Turbomachinery*, Vol. 123, pp. 709-719.

[17] Nicklas, M., 2001, "Film-Cooled Turbine Endwall in a Transonic Flow Field: Part II-Heat Transfer and Film-Cooling Effectiveness," *J of Turbomachinery*, Vol. 123, pp. 720-729.

[18] Kost, F. and Mullaert, A., 2006, "Migration of Film-Coolant from Slot and Hole Ejection at a Turbine Vane Endwall," ASME Paper GT2006-90355.

[19] Cardwell, N.D., Sundaram, N., and Thole, K.A., 2006, "The Effects of Varying the Combustor-Turbine Gap," ASME Paper GT2006-90089.

[20] Lynch, S.P., and Thole, K.A., 2007, "The Effects of Combustor-Turbine Interface Gap

Leakage on the Endwall Heat Transfer for a Nozzle Guide Vane," ASME Paper GT2007-27867.

[21] Munson, B.R., Young, D.F., and Okiishi, T.H., 2002, *Fundamentals of Fluid Mechanics* (4th ed.), New York: John Wiley & Sons, Inc., p. 514.

[22] Naughton, J.W. and Sheplak, M., 2002, "Modern developments in shear stress measurement," *Progress in Aerospace Sciences*, Vol. 38, pp. 515-570.

[23] Harrison, S., 1990, "Secondary Loss Generation in a Linear Cascade of High-Turning Turbine Blades," *J of Turbomachinery*, Vol. 112, pp. 618-624.

[24] Holley, B., and Langston, L.S., "Surface Shear Stress and Pressure Measurements in a Turbine Cascade," GT2006-90580.

[25] Moffat, R. J., 1988, "Describing the Uncertainties in Experimental Results," *Experimental Thermal and Fluid Science*, Vol. 1, pp. 3-17.

[26] FLUENT (version 6.2.1), Fluent Inc., Lebanon, NH.

**Table 2.1 Vane Geometry and Flow Conditions**

| | |
|---|---|
| Scaling factor | 9 |
| Scaled vane chord (C) | 59.4 cm |
| Axial chord/chord ($C_{ax}$/C) | 0.48 |
| Pitch/chord (P/C) | 0.77 |
| Span/chord (S/C) | 0.93 |
| Inlet Reynolds number ($Re_{in}$) | $2.2x10^5$ |
| Inlet mainstream velocity ($U_{\infty,in}$) | 6.3 m/s |
| Inlet, exit angle | 0°, 78° |
| Inlet, exit Mach number | 0.017, 0.085 |

**Table 2.2 Leakage Flow Coolant Settings**

| Slot width | MFR | M | I |
|---|---|---|---|
| Nominal | 0.5% | 0.19 | 0.03 |
| Half | 0.5% | 0.36 | 0.13 |
| Nominal | 1.0% | 0.36 | 0.13 |
| Half | 1.0% | 0.73 | 0.50 |

**Table 2.3 Endwall and Fillet Geometry**

| | Parameter | Value |
|---|---|---|
| Upstream slot | A – Location upstream of vane | 0.37C (0.77$C_{ax}$) |
| | B – Width (nominal / half) | 0.024C / 0.012C |
| | D – Flow length (nominal / half) | 1.88B / 3.76B |
| | E – Injection angle | 45° |
| Leading edge fillet | F – Fillet LE to upstream slot | 0.18C (0.38$C_{ax}$) |
| | G – Maximum extent of fillet | 0.16C |
| | H – Location of max. extent, relative to vane stagnation | 0.057C |
| | I – Maximum distance around PS | -0.87C |
| | J – Maximum distance around SS | 0.57C |
| | K – Maximum height of fillet | 0.16C |

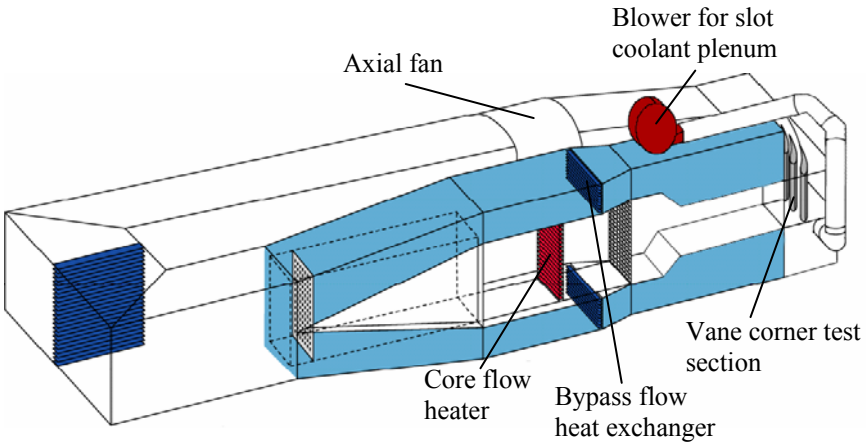


**Figure 2.1 Depiction of the closed loop wind tunnel used in this study.**

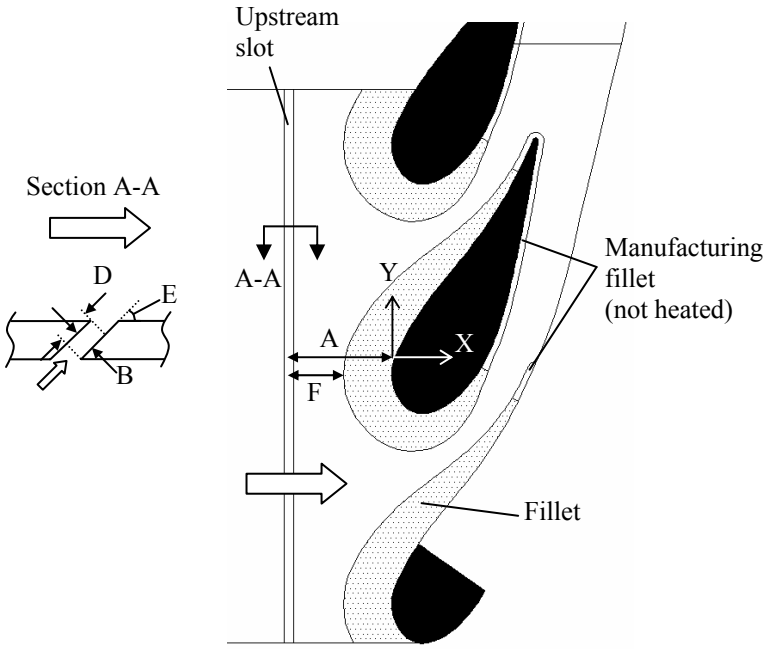


**Figure 2.2 Schematic of the endwall and combustor-turbine interface gap (upstream slot) modeled in this study.**

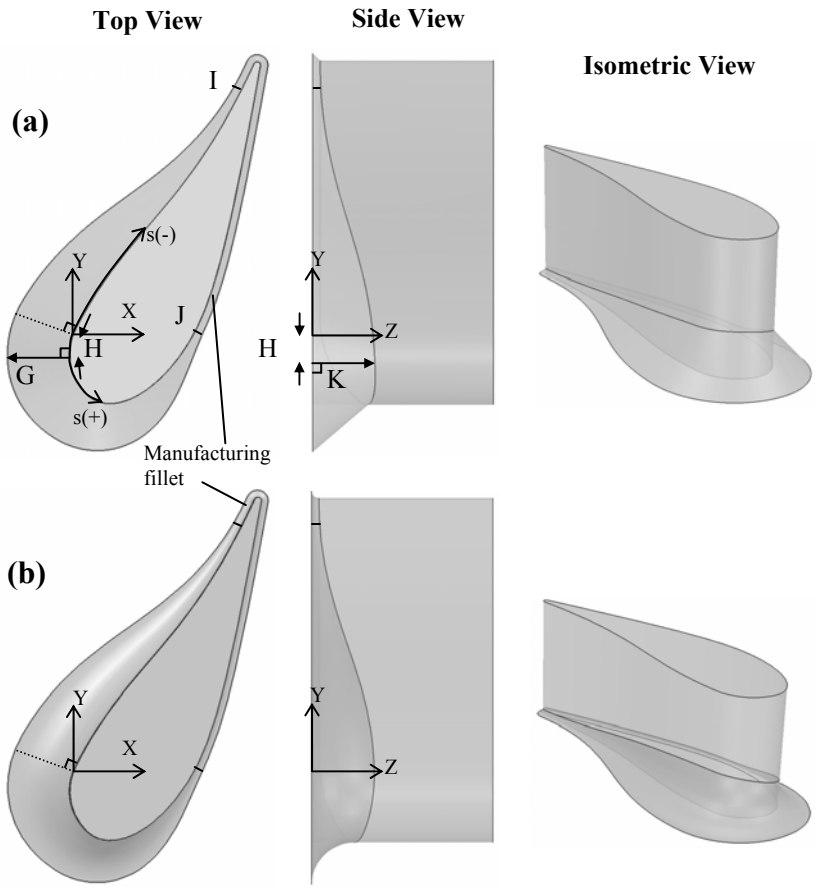


**Figure 2.3 Geometrical parameters for an endwall-airfoil fillet with (a) a linear profile, and (b) an elliptical profile.**

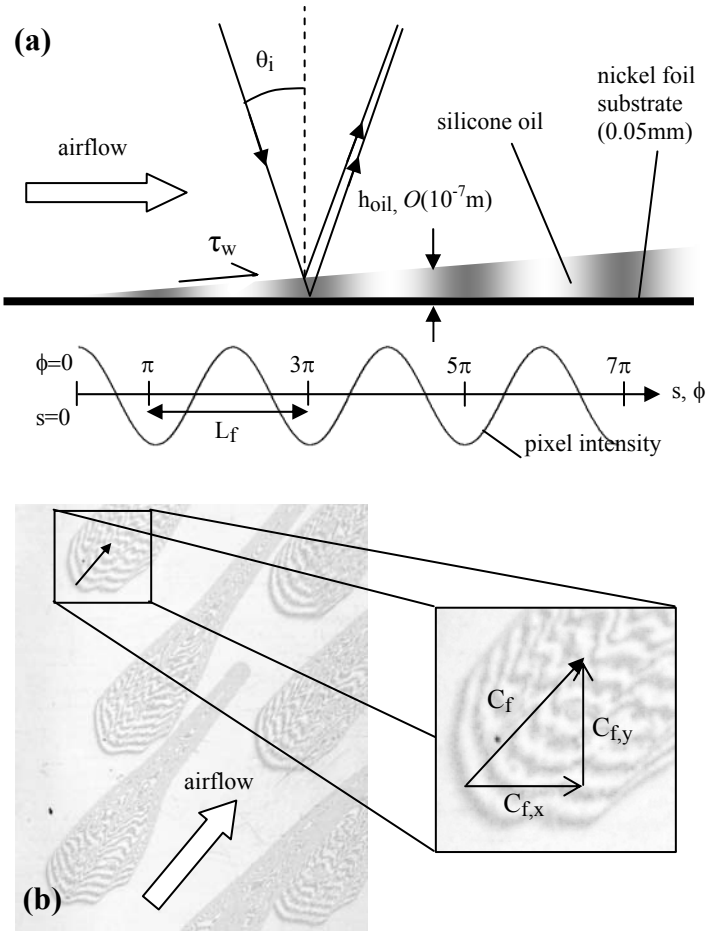


**Figure 2.4** **Schematic of oil film development due to shear (a); and a sample interferogram (b) which demonstrates friction coefficient directionality.**

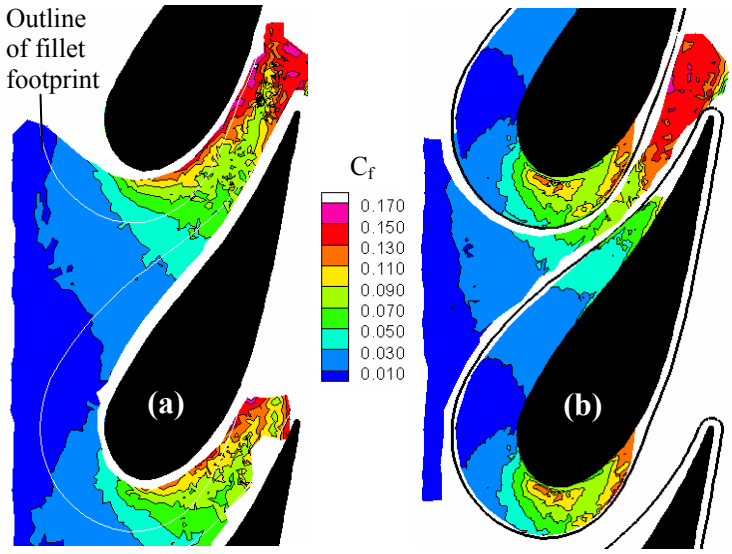


**Figure 2.5** **Friction coefficient magnitude for a vane with (a) no fillet, and with (b) a linear fillet.**

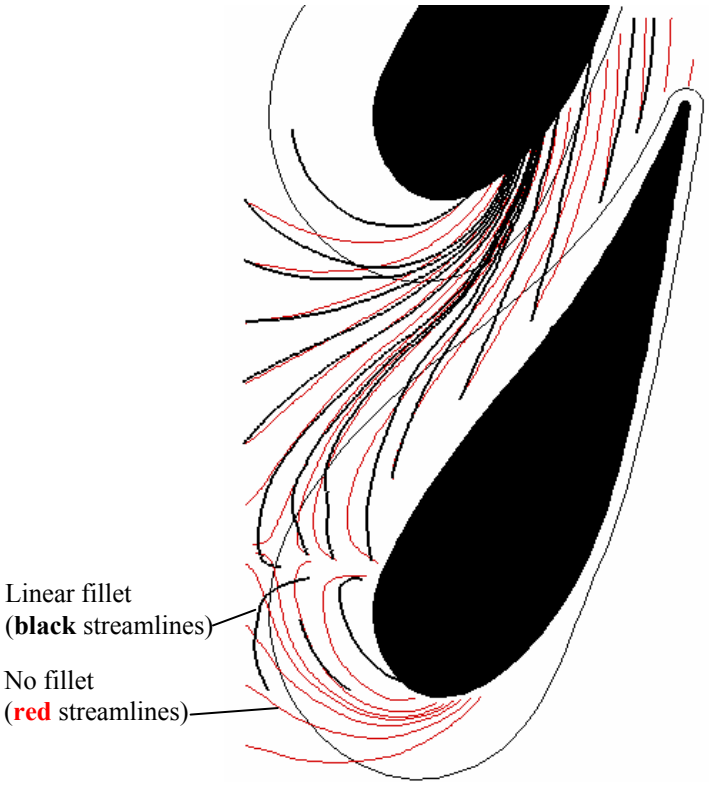


**Figure 2.6** **Endwall streamlines for the linear fillet (black), overlaid with unfilleted endwall streamlines (red). Streamlines were calculated from the surface shear stress measurements.**

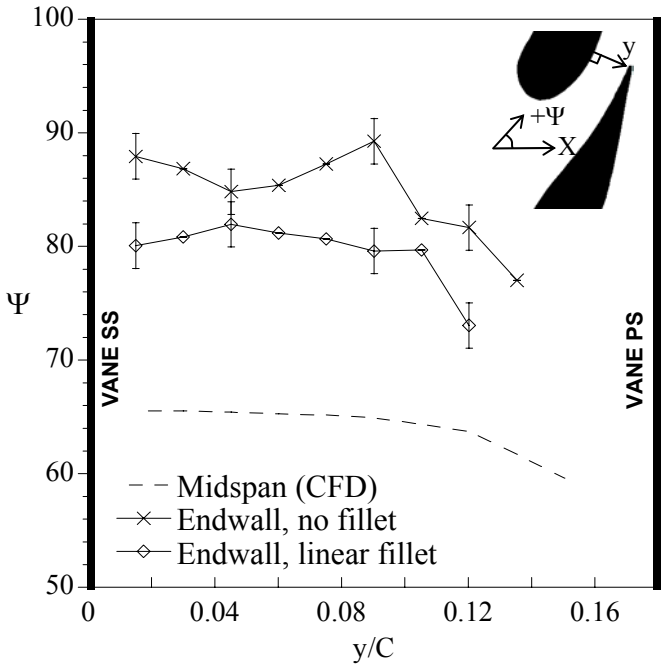


**Figure 2.7** **Yaw angle of endwall streamlines at the throat compared to inviscid streamlines, indicating reduced overturning for a vane with a linear fillet.**

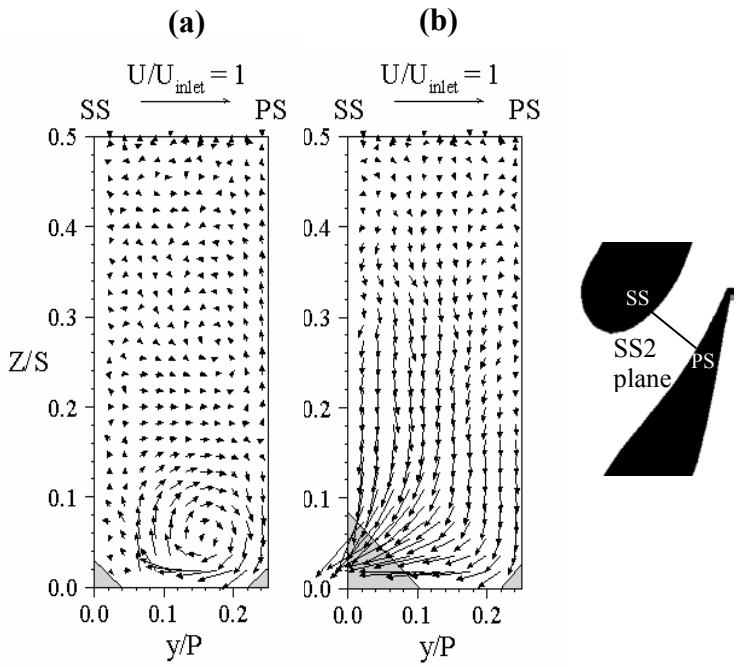


**Figure 2.8** **Computed flowfield results of Lethander et al. [6] at plane SS2 with (a) no fillet, and (b) the linear fillet.**

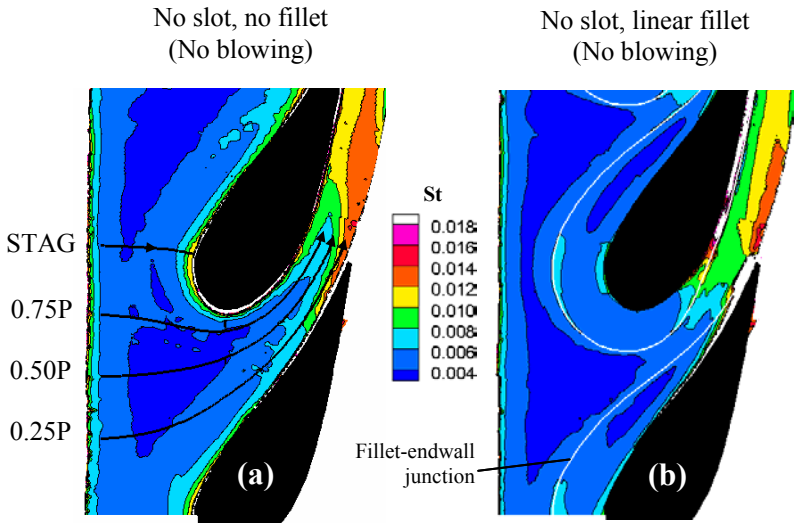


**Figure 2.9** **Heat transfer coefficient contours for the endwall (a) without a fillet, and (b) with the linear fillet. Inviscid streamline paths are overlaid on (a).**

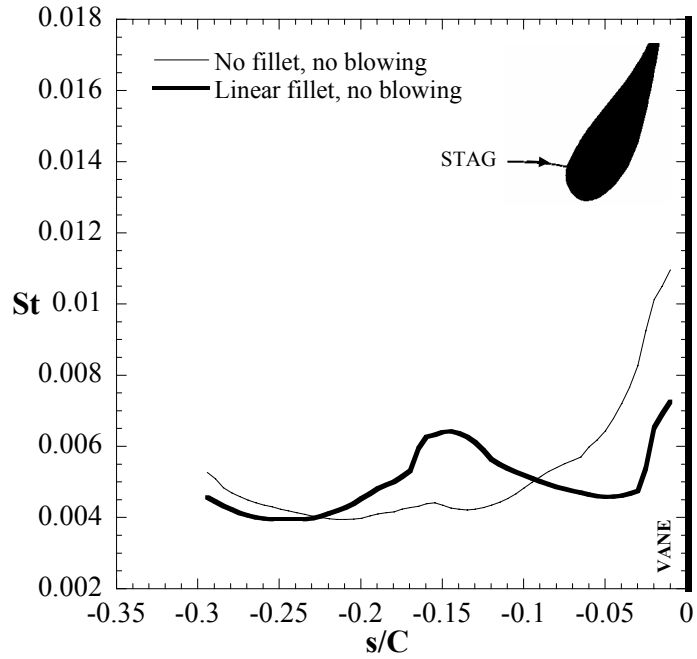


**Figure 2.10 Heat transfer coefficients without upstream slot blowing, extracted along the inviscid streamline approaching the vane stagnation (see Figure 2.9a).**

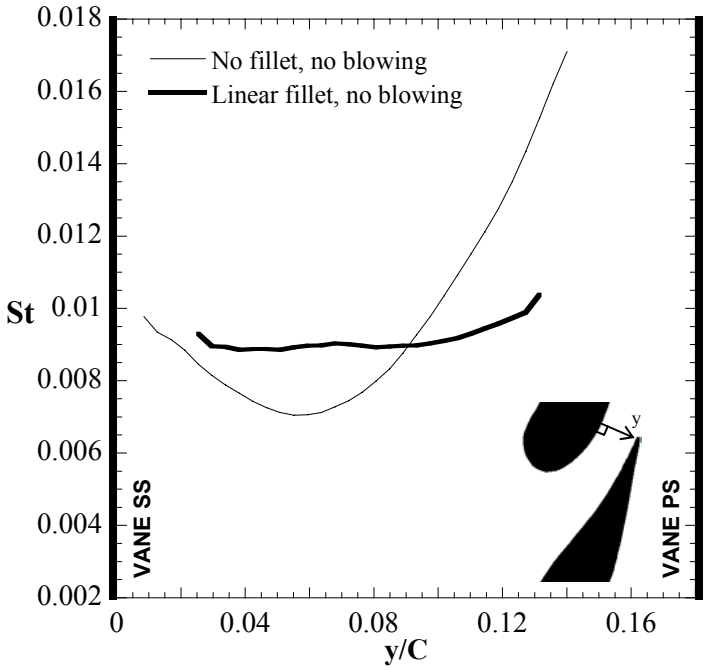


**Figure 2.11 Heat transfer coefficients at the throat for no upstream slot blowing.**

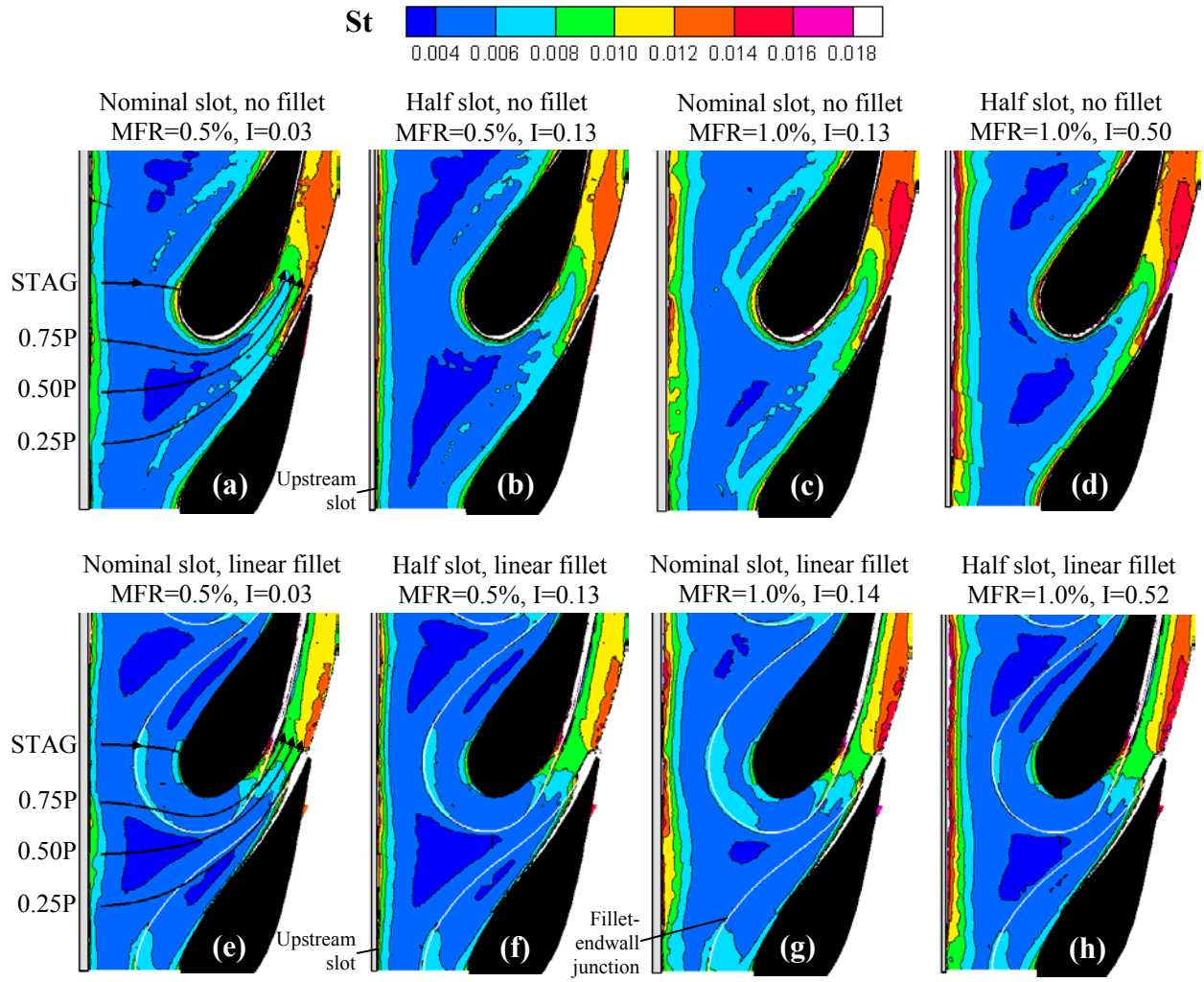


**Figure 2.12 Heat transfer coefficient contours for the various upstream slot flow rates and widths, for the endwall without a fillet (a-d) and the endwall with a linear fillet (e-h).**

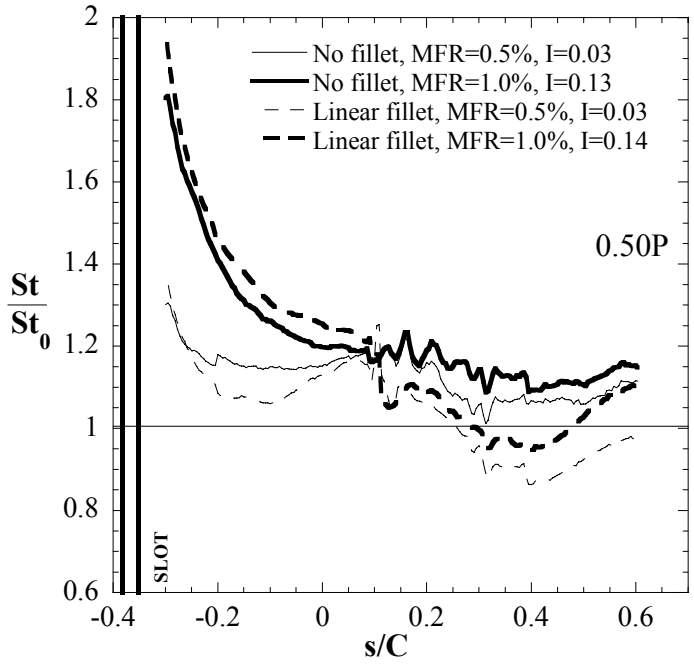


**Figure 2.13 Heat transfer augmentation relative to the no-blowing cases, extracted along the 0.50P streamline path, for increased slot mass flow through the nominal slot.**

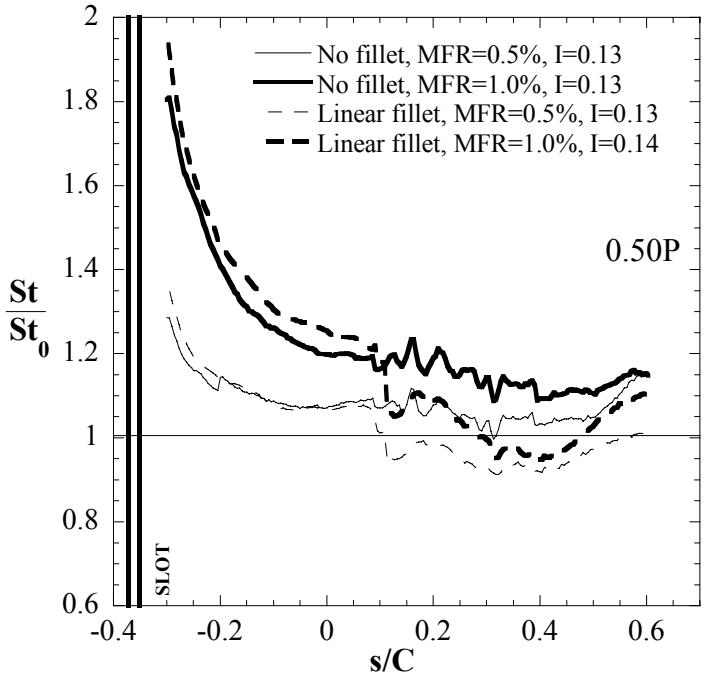


**Figure 2.14 Heat transfer augmentation along the 0.50P streamline path for matched slot momentum flux from the nominal and half slots.**

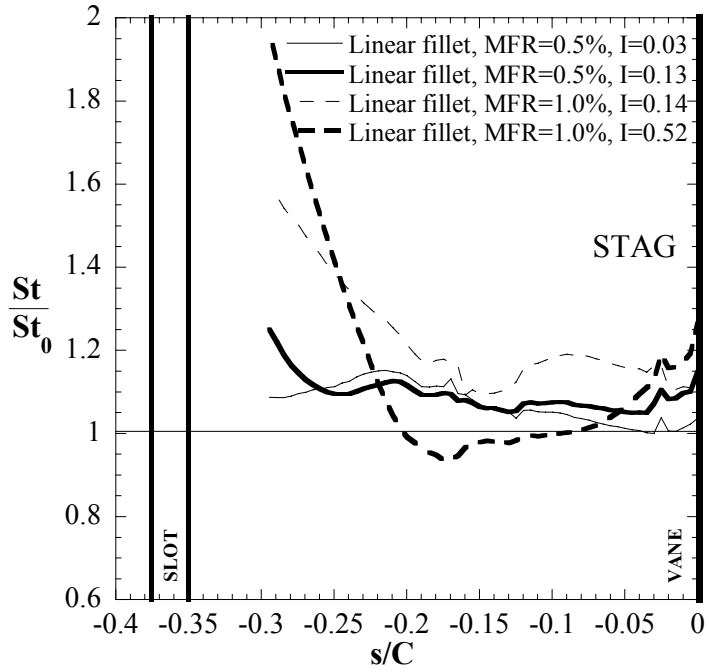


**Figure 2.15 Heat transfer augmentation for the linear fillet along the inviscid stagnation (STAG) streamline path.**

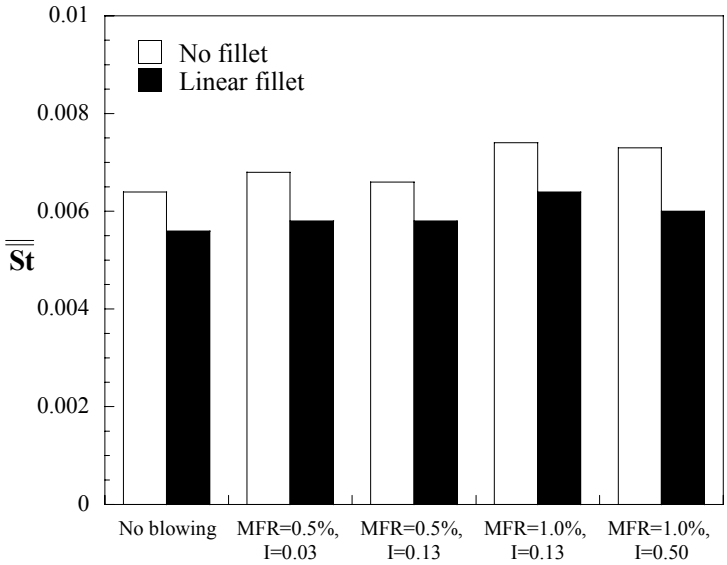


**Figure 2.16 Comparison of area-averaged heat transfer for the various upstream slot leakage flow conditions.**

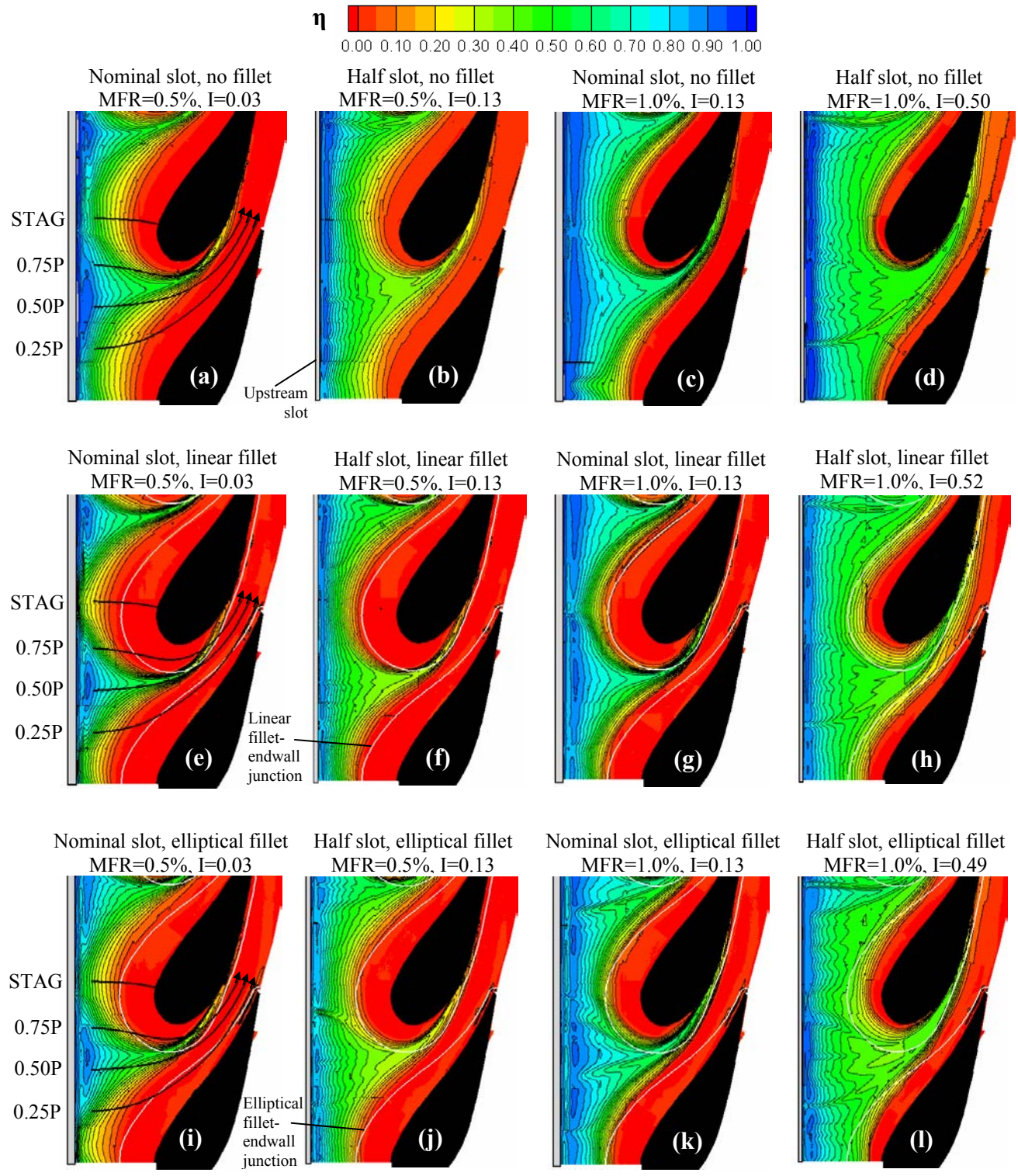


**Figure 2.17 Adiabatic cooling effectiveness contours for the various upstream slot flow rates and widths, for an airfoil with no fillet (a-d), a linear fillet (e-h), and an elliptical fillet (i-l).**

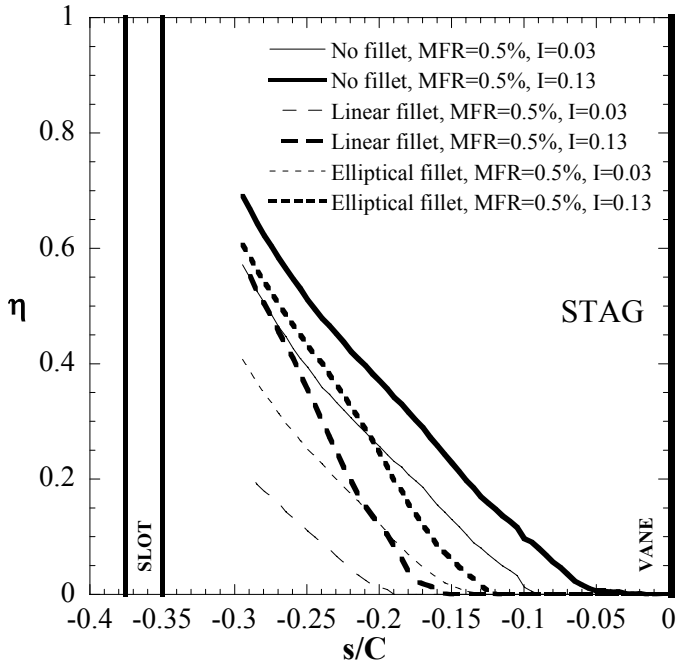


**Figure 2.18 Adiabatic cooling effectiveness for low slot leakage mass flow, along the inviscid streamline path approaching the vane stagnation.**

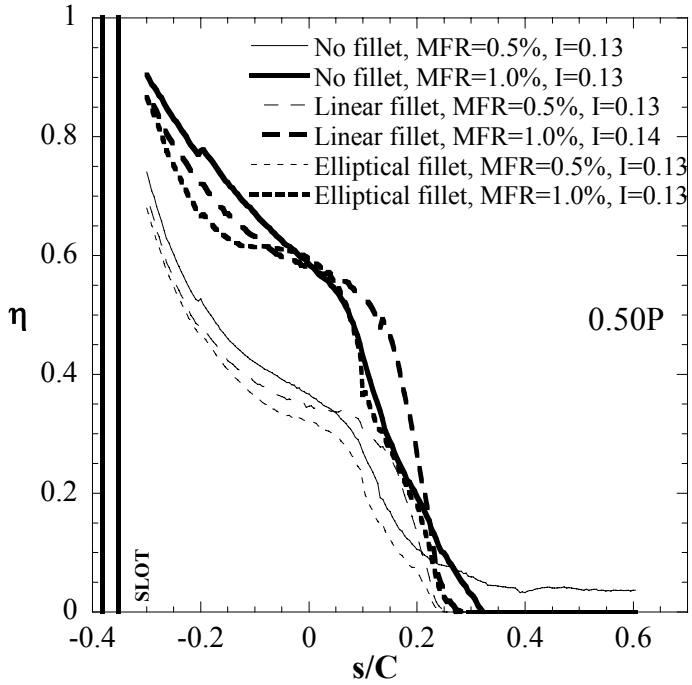


**Figure 2.19 Cooling effectiveness levels extracted along the 0.50P streamline for matched slot momentum flux ratio.**

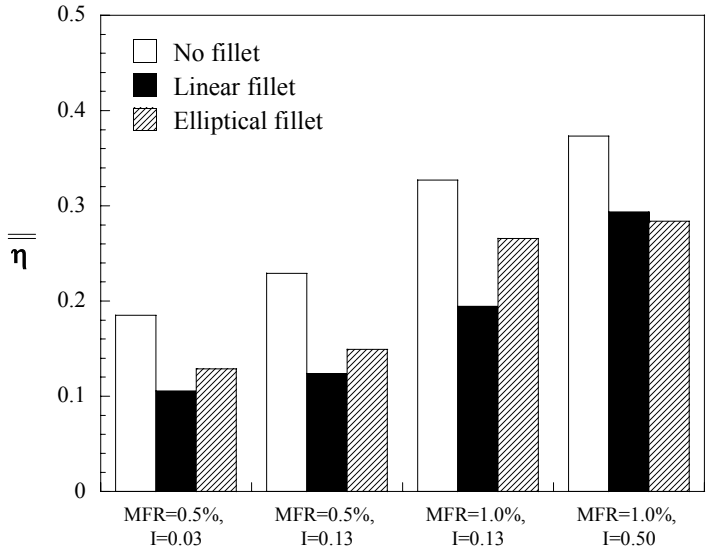


**Figure 2.20 Area-averaged adiabatic cooling effectiveness of leakage flow from an upstream slot, for an airfoil with no fillet, a linear fillet, or an elliptical fillet.**